
Universidade de Aveiro Departamento de Física,
2014

Edgar A. P. Wright

Algoritmo Genético para fiber-FROG com Propagação Simulada de Pulsos

Genetic Algorithm for fiber-FROG using Simulated Pulse Propagation

Edgar A. P. Wright

Algoritmo Genético para fiber-FROG com Propagação Simulada de Pulsos

Genetic Algorithm for fiber-FROG using Simulated Pulse Propagation

Dissertação apresentada à Universidade de Aveiro para cumprimento dos requesitos necessários à obtenção do grau de Mestre em Física, realizada sob a orientação científica da Professora Doutora Margarida Maria Resende Vieira Facão, Professora Auxiliar do Departamento de Física da Universidade de Aveiro e a co-orientação científica do Professor Doutor Armando Humberto Moreira Nolasco Pinto, Professor Associado do Instituto de Telecomunicações de Aveiro.

o júri/the jury

presidente/president	**Professor Doutor Ricardo Assis Guimarães Dias** Professor Auxiliar, Universidade de Aveiro
vogais/examining committee	**Professor Doutor Ariel Ricardo Negrão da Silva Guerreiro** Professor Auxiliar, Universidade do Porto - Faculdade de Ciências
	Professora Doutora Margarida Maria Resende Vieira Facão Professora Auxiliar, Universidade de Aveiro

agradecimentos

Agradeço à Professora Margarida, ao Gil, ao Ricardo, ao Álvaro, ao Ali, ao Sr. Ivo, ao Sr. Miguel e a todas as restantes pessoas que interagiram comigo ao longo dos últimos 9 meses. Obrigado pela experiência.

palavras-chave FROG, fibre-FSR, fibre-FROG, Algoritmo Genético

resumo Nesta tese é implementado um algoritmo genético para fazer uma reconstrução de fase a duas dimensões com base na variante da técnica de frequency-resolved optical gating conhecida como fibre-FROG. Um novo parâmetro, denominado fibre-FSR, é proposto com o intuito de melhorar a convergência do algoritmo, e testado para 9 pulsos com parâmetros time-bandwidth product compreendidos entre 0.604 e 7.047. Dois destes pulsos, centrados em $1556\,\mathrm{nm}$, com uma largura a meia altura de $100\,\mathrm{fs}$ e uma energia de $24\,\mathrm{pJ}$ são também reconstruídos resolvendo numericamente, a cada iteração do algoritmo, as equações de propagação para $2\,\mathrm{m}$ de dispersion-shifted fibre com $\gamma = 2.36\,\mathrm{W^{-1}\,km^{-1}}$ e $\beta_2 = -804.78\,\mathrm{fs^2\,m^{-1}}$.

keywords FROG, fibre-FSR, fibre-FROG, Genetic Algorithm

abstract In this thesis a genetic algorithm for two dimensional phase reconstruction is implemented, based on frequency-resolved optical gating using the fibre-FROG geometry. A new parameter, termed fibre-FSR, is proposed to improve the algorithm's convergence, and tested for 9 pulses with time-bandwidth products between 0.604 and 7.047. Two of these pulses, centred about $1556\,\mathrm{nm}$, with a full width at half maximum of $100\,\mathrm{fs}$ and an energy of $24\,\mathrm{pJ}$ are also reconstructed solving the pulse's propagation equations numerically at each iteration in the algorithm, over $2\,\mathrm{m}$ of dispersion-shifted fibre with $\gamma = 2.36\,\mathrm{W^{-1}\,km^{-1}}$ and $\beta_2 = -804.78\,\mathrm{fs^2\,m^{-1}}$.

Contents

List of Figures

List of Tables

Acronyms

B bandwidth
DFT discrete fourier transform
DSF dispersion-shifted fibre
GA genetic algorithm
GDD group delay dispersion
GP generalised projections
GV group velocity
GVD group velocity dispersion
FROG frequency-resolved optical gating
FSR FROG sampling rate
FT fourier transform
FWHM full width half maximum
IFT inverse fourier transform
RMS root mean squared
SPM self phase modulation
T RMS width
TBP time-bandwidth product
XPM cross phase modulation

Chapter 1

Introduction

An ultrashort pulse is a short burst of electromagnetic radiation, with a temporal duration of tens of picoseconds or less. Ultrashort pulses as short as 6 ps were produced as early as 1967, and sub-100 fs ultrashort pulses as early as 1981 [1]. In 2001 the minimum temporal duration of ultrashort pulses was further shortened with the generation of the first attosecond pulse [2].

Many interesting processes in nature occur on time scales which are only made accessible to experimentalists using ultrashort pulses. The latter are routinely used to study carrier dynamics in photoexcited semiconductors, where the relevant processes, such as phonon scattering, occur on time scales ranging from approximately 10 ps to 10 fs [3, 4]. Applications in other fields such as Biology and Chemistry include the study of protein folding mechanisms [5], and the spectroscopy of electronic couplings in photosynthesis [6], on picosecond and femtosecond time scales. Beyond the molecular length scale, attosecond ultrashort pulses have been used to study electronic processes on an atomic scale [7].

In addition to their temporal resolving power in optical pump-probe type experiments, ultrashort pulses are also useful tools for studying nonlinear phenomena in dielectrics. With energies as low as 24 pJ [8], these short pulses have enough peak intensity to produce a nonlinear response in dielectric media such as silica. Not only do nonlinear effects in silica impose power and bandwidth limitations on fiber-optical communications systems [9] but they also enable technologies for pulse shaping/tailoring [10, 11] and increased data throughput [12].

Accurately determining the short temporal duration and intensity profiles of ultrashort pulses is essential to the aforementioned applications, yet hindered by the very limitations which motivate the use of ultrashort pulses in some of those applications: resolving an event in time requires another event in time which is as short or shorter.

Although recent work is pushing the limits of optoelectronic response times to subpicosecond time scales, such response times only became available as recently as 2013 [13], and much shorter pulses, which require characterization, had already been created by then. As a copy of a pulse is as short as the pulse itself, autocorrelation techniques were employed in the time and frequency domains to characterise ultrashort pulses [14]. Building on these autocorrelation techniques frequency-resolved optical gating (FROG) was created by Trebino et al. [15], by resolving the intensity autocorrelation in frequency. This was shown to be equivalent to a short-time fourier transform, resulting in a two-

dimensional representation of the pulse, in the time-frequency domain, termed the FROG trace. The retrieval of the pulse's amplitude and phase from the FROG trace was then shown to be equivalent to a two-dimensional phase reconstruction problem [16]. Various algorithms have been proposed and used successfully to perform a FROG phase-reconstruction, such as the generalised projections algorithm, the principle-component generalised projections algorithm and genetic algorithms [17–21]. There are various types of setup for obtaining FROG traces, providing different sensitivities in function of the nonlinearities which are exploited to produce the FROG trace [16]. Addressing the increasing demand for characterising ultrashort pulses at the wavelength used in optical communications systems Thomson et al. [8] proposed a type of frog termed fibre-FROG. This FROG geometry has since been extended to use optical fibres with a higher non-linearity, enabling the characterisation of pulses with even lower energies for a temporal duration of about 5 ps [22].
The original aim of this thesis was to extend existing work on fibre-FROG by characterising a pulse with a temporal duration of about 100 fs. Due to experimental constraints, specifically the length of SMF28 (single-mode fibre) patch cords, the need arose to take dispersion into account during reconstruction. Using traces produced by a fibre-FROG setup containing a highly birefringent microstructured optical fibre (MOF) Vrany et al. [21] reported some success reconstructing pulses with a duration of 555 fs. The reconstruction was performed using a Genetic Algorithm (GA) instead of Generalised Projections (GP), as the latter had failed to perform well due to the added birefringence. Given the prior successful usage of GA with FROG [19, 21] and the fact that a GA also enables dispersion to be taken into account through the use of pulse propagation simulations, whereas GP does not, a GA was implemented following the work of Vrany et al. [21].

1.1 Thesis Outline

The current work is divided into 4 chapters beside this one. Various broad and comparatively specialised areas of Physics are required in understanding and applying FROG. For this reason the second chapter, titled Utrashort Pulses, is divided into two sections. In the first section fundamentals of time-frequency analysis are introduced. This is followed by a second section where medium nonlinearities are discussed, those of silica in particular, as a prelude to a succinct discussion of the propagation of pulses in a single-mode optical fibre.
The third chapter, titled Frequency-Resolved Optical Gating explains how the pulse characterization problem is framed as a two-dimensional phase reconstruction problem. This is followed by a brief explanation of the fibre-FROG geometry and a discussion of the limitations of acquiring and resolving data for FROG. Finally, a brief explanation of how genetic algorithms work is presented in the context of FROG phase reconstruction.
In the fourth chapter, titled Results and Discussion a thorough testing of the genetic algorithm created for this thesis is presented along with some remarks regarding the results of those tests.
In the final chapter, the results and discussion presented in the previous chapter are summed up and future work proposed.

Chapter 2

Ultrashort Pulses

An ultrashort pulse is a short burst of electromagnetic radiation, usually defined by its electric field $\vec{\mathscr{E}}(\vec{r},t)$ in $\mathrm{V\,m^{-1}}$. In general,

$$\vec{\mathscr{E}}(\vec{r},t) \propto \hat{e}\sqrt{I(\vec{r},t)}\cos(\vec{k}\cdot\vec{r}-\omega_0 t+\phi(t)), \tag{2.1}$$

where $\hat{e}$ is a unit vector, $I(\vec{r},t)$ is defined as the radiant flux (power in W), $\vec{k}$ is the wave vector, $\vec{r}$ the position and ω_0 the carrier frequency in $\mathrm{rad\,s^{-1}}$. Ignoring the spatial dependence of the radiant flux, and considering the ultrashort pulse at some reference position, with its polarization along a single direction it follows that,

$$\mathscr{E}(t) = \sqrt{I(t)}\cos(\phi(t)-\omega_0 t), \tag{2.2}$$

where the proportionality constants were omitted following [14, p.13].
The finite duration of the ultrashort pulse is described by the amplitude $\sqrt{I(t)}$. Over this time, e.g. 1 ps, an ultrashort pulse can oscillate hundreds of times. For example, a near infrared (nIR) ultrashort pulse at $\lambda_0 = 1550\,\mathrm{nm}$, corresponding to $\omega_0 = 1.22{\times}10^{15}\mathrm{rad\,s^{-1}}$ in the vacuum, completes each cycle of oscillation in approximately 5.19 fs, oscillating approximately 19.2 times in 100 fs. More generally, the number of periods of oscillation may change over time, which is taken into account by $\phi(t)$, and will be discussed further in subsection §2.1.1.

2.1 Introducing the Time-Frequency Domain

Time-varying signals such as $\mathscr{E}(t)$ are normally represented in the time-domain, lending themselves to calculations of the energy they contain. However, these signals may also be represented in the frequency domain, simplifying differential equations or providing a better framework for describing physical phenomena such as dispersion (as will be discussed in section §2.2). Mathematically both representations are related by a FT, such that $\mathscr{E}(\omega) = \mathscr{F}\{\mathscr{E}(t)\}$, or by an IFT, such that $\mathscr{E}(t) = \mathscr{F}^{-1}\{\mathscr{E}(\omega)\}$. It is noted that the following FT and IFT definitions are employed throughout this work,

$$\mathscr{E}(\omega) = \int \mathrm{dt}\ \mathscr{E}(t)\,\mathrm{e}^{i\omega t}, \tag{2.3a}$$

$$\mathscr{E}(t) = \frac{1}{2\pi}\int \mathrm{d}\omega\, \mathscr{E}(\omega)\, \mathrm{e}^{-i\omega t}, \tag{2.3b}$$

respectively, in accordance with the sign convention adopted in equation (2.1). It is also noted that all integrals are taken between $-\infty$ and $+\infty$ unless stated otherwise.

The idea of interpreting signals such as $\mathscr{E}(t)$ in both time and frequency, based on physical arguments, was first proposed by Gabor [23] who noted the connection between such an interpretation and the formalism of quantum mechanics. To leverage the latter he proposed what is known as the analytic signal representation. In essence, it was proposed that the real-valued signal $\mathscr{E}(t)$ oscillating in time be converted to the complex-valued signal $E(t)$ rotating in the complex plane, such that $E(t) = \mathscr{E}(t) + i\sigma(t)$, where $\sigma(t)$ is proportional to the hilbert transform of $\mathscr{E}(t)$ [24, p. 14]. The spectral version of the analytic signal is written

$$E(\omega) = \sqrt{S(\omega)}\, \mathrm{e}^{i\Phi(\omega)}, \tag{2.4}$$

defining the pulse's spectral power $S(\omega)$ and the spectral phase $\Phi(\omega)$. Equivalently, the IFT of equation (2.4), often termed the complex amplitude, is expressed

$$E(t) = \sqrt{I(t)}\, \mathrm{e}^{i\phi(t)}, \tag{2.5}$$

defining the phase $\phi(t)$.

Comparing the phases in equations (2.2) and (2.5) shows the latter ignores a multiplicative carrier term $\mathrm{e}^{-i\omega_0 t}$, a matter of convenience justified by the IFT shift theorem: $\mathscr{F}^{-1}\left\{E(\omega-\omega_0)\right\} = \mathrm{e}^{-i\omega_0 t}\, E(t)$. The carrier term simply causes a shift in the spectrum, leaving it otherwise unaltered and is thus omitted from the analytic signal. The power, and phase are readily computed from equation (2.5), such that $I(t) = |E(t)|^2$, and $\phi(t) = \mathrm{Im}\{\ln[E(t)]\}$, as are the spectral power and the spectral phase from equation (2.4).

2.1.1 Phase, Group Delay and Instantaneous Frequency

To better understand how the phase characterises the pulse the former is expanded as a Taylor series, about the carrier frequency, so that

$$\Phi(\omega) = \Phi_0^{(0)} + (\omega-\omega_0)\Phi_0^{(1)} + \frac{1}{2}(\omega-\omega_0)^2\Phi_0^{(2)} + \frac{1}{6}(\omega-\omega_0)^3\Phi_0^{(3)} + \cdots + \frac{1}{n!}(\omega-\omega_0)^n\Phi_0^{(n)}, \tag{2.6}$$

where $\Phi_0^{(0)} = \Phi(\omega_0)$, the zero-order spectral phase, and $\Phi_0^{(n)} = \left.\frac{\mathrm{d}^n\Phi(\omega)}{\mathrm{d}\omega^n}\right|_{\omega_0}$, the n-order spectral phase.

The zero-order spectral phase, termed absolute phase, is a constant so $\Phi_0^{(0)} = \phi_0^{(0)}$, which follows from the linearity of the FT integral, where $\phi_0^{(0)}$ is the zero order phase, in an expansion of $\phi(t)$ about t_0:

$$\phi(t) = \phi_0^{(0)} + (t-t_0)\phi_0^{(1)} + \frac{1}{2}(t-t_0)^2\phi_0^{(2)} + \frac{1}{6}(t-t_0)^3\phi_0^{(3)} + \cdots + \frac{1}{n!}(t-t_0)^n\phi_0^{(n)}. \tag{2.7}$$

By recalling equations (2.5) and (2.2), and representing the former in the complex plane, it follows that the zero-order phase represents the phase between the amplitude and the carrier, at a particular time.

Analogously to the discussion concerning the absence of the carrier term in equation (2.5), the FT shift theorem states that $\mathscr{F}\{E(t-\tau)\} = \mathrm{e}^{i\omega\tau}\,E(\omega)$, so it follows that the first-order spectral phase describes a temporal shift in the amplitude, in the same way the first-order phase represents a frequency shift in spectral amplitude.

The variables ω and t can be represented as operators in the time and frequency domains respectively [25]:

$$\mathscr{W} = i\frac{\mathrm{d}}{\mathrm{dt}}, \tag{2.8a}$$

and

$$\mathscr{T} = -i\frac{\mathrm{d}}{\mathrm{d}\omega}. \tag{2.8b}$$

Expectation values can then be calculated using a formalism similar to that of quantum mechanics, such that

$$\langle \mathrm{g}(t)\rangle = \int \mathrm{d}\omega\, E^*(\omega)\mathrm{g}\left(-i\frac{\mathrm{d}}{\mathrm{d}\omega}\right)E(\omega), \tag{2.9a}$$

and

$$\langle \mathrm{h}(\omega)\rangle = \int \mathrm{dt}\, E^*(t)\mathrm{h}\left(i\frac{\mathrm{d}}{\mathrm{dt}}\right)E(t), \tag{2.9b}$$

where $\mathrm{g}(t)$ and $\mathrm{h}(\omega)$ are generic functions of time and angular frequency respectively, where $\int \mathrm{dt}\, I(t) = \int \mathrm{d}\omega\, S(\omega) = 1$ [26, p.947]. The total energy of the pulse is $E_T = \int \mathrm{dt}\,|E(t)|^2$ and, from Parseval's Theorem, $E_T = \frac{1}{2\pi}\int \mathrm{d}\omega\,|E(\omega)|^2$. This is in line with equations (2.5) and (2.4), and shows $I(t)$ and $S(\omega)$ can be used to calculate statistical quantities, e.g. $\langle\omega\rangle = \int \mathrm{d}\omega\,\omega S(\omega)/\int \mathrm{d}\omega\, S(\omega)$. Such calculations can also be performed using equations (2.9a) and (2.9b), with the added advantage that all calculations can be performed exclusively in either domain.

Applying equation (2.9b) to calculate the expectation value of the angular frequency yields

$$\langle\omega\rangle = -\int \mathrm{dt}\,\frac{\mathrm{d}\,\phi(t)}{\mathrm{dt}}I(t). \tag{2.10}$$

Equation (2.10) lends itself to the definition of an instantaneous frequency for the pulse ω_{inst} such that

$$\omega_{\mathrm{inst}} \equiv -\frac{\mathrm{d}\,\phi(t)}{\mathrm{dt}}. \tag{2.11}$$

A similar argument using equation (2.9a) to calculate the expectation value for the time, leads to the definition of a time delay for a particular frequency, normally termed the group delay, t_{group}, such that

$$t_{\mathrm{group}} \equiv \frac{\mathrm{d}\,\Phi(\omega)}{\mathrm{d}\omega}. \tag{2.12}$$

Applying equation (2.11) to $\phi(t)$, up to second order in the series expansion, shows $\omega_{\mathrm{inst}} = -\phi_0^{(2)}t$ where t_0 has been set to 0 s for simplicity. Thus, the second order phase describes what is termed a linear chirp, i.e. a linear change in the instantaneous frequency with time. A similar argument concerning the second-order spectral phase (cf. equation (2.14)) shows the latter describes a linear temporal delay to different frequency components of the pulse [27]. In general, the n^{th} order of the

phase and spectral phase will each contribute a change, of order $n-1$ in time and frequency, to the instantaneous frequency and to the group delay respectively, such that

$$\omega_{\text{inst}} = \sum_{n=2}^{\infty} \frac{n}{n!} \phi_0^{(n)} t^{n-1}, \tag{2.13}$$

and

$$t_{\text{group}} = \sum_{n=2}^{\infty} \frac{n}{n!} \Phi_0^{(n)} \omega^{n-1}. \tag{2.14}$$

2.1.2 Time-Bandwidth Product

The physical interpretation of all phase terms has followed more or less directly from the properties of FTs as well as from the $\mathscr{T}$ and $\mathscr{W}$ operators. It is therefore reasonable to derive a measure of the information present in the pulse from the analysis of the properties of FT-pairs.
A well-known result relating non-commutable variables, which are FT conjugates, is the uncertainty principle:

$$\sigma_t \sigma_\omega \geq \frac{1}{2} \sqrt{|\langle [\mathscr{T}, \mathscr{W}] \rangle|^2 + 4\text{Cov}_{t\omega}^2}, \tag{2.15}$$

where σ_t and σ_ω are temporal and spectral standard deviations respectively and $\text{Cov}_{t\omega} = \langle t\omega \rangle - \langle t \rangle \langle \omega \rangle$ is the covariance. Replacing $\mathscr{T}$ with t in the commutator $[\mathscr{T}, \mathscr{W}]$, and applying the former to a generic function of time yields $[\mathscr{T}, \mathscr{W}] = i$ so that $|\langle [\mathscr{T}, \mathscr{W}] \rangle|^2 = 1$. This shows that the dimensionless constant $\sigma_t \sigma_\omega$ has its lower bound determined by $\text{Cov}_{t\omega}^2$, increasing as the correlation (or the anticorrelation) between t and ω increases.
The standard deviation is a measure of a probability distribution's spread around an average value so σ_t and σ_ω are in this sense a measure of the width of $I(t)$ and $S(\omega)$, i.e. a measure of a pulse's temporal and spectral widths. The standard deviation is often called the RMS width in the sense that it is the square root of the mean of the square of the difference between an independent variable x and its expectation value, usually interpreted as a baseline [14]. Mathematically, $\sigma_x = \sqrt{\left\langle (x^2 - \langle x \rangle)^2 \right\rangle}$. By defining T as the RMS temporal width of a pulse and B as its bandwidth (RMS spectral width) $\sigma_t \sigma_\omega = TB$ which is known as the time-bandwidth product (TBP). From the previous analysis of equation (2.15) it is clear that a pulse cannot be arbitrarily small in both time and frequency, and the lower bound of the TBP increases with the correlation (or anticorrelation) between time and frequency.
From equation (2.9b) and all the relevant definitions it follows that

$$\text{B} = \sqrt{\int \text{dt} \left(\frac{\text{d}}{\text{dt}} \sqrt{I(t)} \right)^2 + \int \text{dt} \left(\frac{\text{d}}{\text{dt}} \phi(t) + \langle \omega \rangle \right)^2 I(t)}. \tag{2.16}$$

Analogously, from equation (2.9a), it follows that

$$\text{T} = \sqrt{\int \text{d}\omega \left(\frac{\text{d}}{\text{d}\omega} \sqrt{S(\omega)} \right)^2 + \int \text{d}\omega \left(\frac{\text{d}}{\text{d}\omega} \Phi(\omega) - \langle t \rangle \right)^2 S(\omega)}. \tag{2.17}$$

Analysing expression (2.16) shows that B is smallest for a constant phase, as $\frac{\mathrm{d}}{\mathrm{dt}}\phi_{\text{constant}} = 0$. Recalling that a constant phase implies an equally constant spectral phase, T is also as small as possible, as shown by equation (2.17). From the definition of $\mathrm{Cov}_{t\omega}$, and using equations (2.9a) and (2.9b), it follows that such a pulse is characterised by a TBP of $\frac{1}{2}$. This is a trivial case of a bandwidth-limited pulse, defined such that T is as short as possible for a particular bandwidth.

2.1.3 The Spectrogram

The TBP has been presented as a reasonable measure of pulse structure, limited by a lower bound which increases as the correlation or anticorrelation between ω and t increases.While such a relationship does not imply causality it motivates, in part, the time-frequency representation of a pulse. Such a representation is further motivated by considering that information such as that provided by the group delay (cf. equation (2.12)), which results from considering the pulse in the frequency domain only, is only true on average. A time-frequency representation is useful in that it is localised in both time and frequency, providing answers to questions such as: What is the spectral composition of the pulse at a given point in time? At what times is a particular frequency present? In essence, the goal is to represent the pulse in a way that combines spectral and temporal information in a single representation [24].

Just like $I(t)$ and $S(\omega)$ are energy densities, such that the integration of either in its respective dimension yields the energy of the pulse, a time-frequency representation of the pulse must be described by a bivariate density $P(t, \omega)$, whose bidimensional integral is also equal to the energy of the pulse. Moreover, if the integral of $P(t, \omega)$ in t or ω yields $S(\omega)$ and $I(t)$ respectively the bidimensional-integration restraint on $P(t, \omega)$ is automatically guaranteed as are the statistical properties associated with the univariate densities [25, p.83-92].

Another reasonable restraint is to guarantee that $P(t, \omega)$ is null when $I(t)$ is null and/or when $S(\omega)$ is null. However mathematically useful and physically reasonable the imposed restraints may be, they do not guarantee the uniqueness of $P(t, \omega)$, nor that the latter's statistical properties lend themselves to physical interpretation, so $P(t, \omega)$ has to be constructed on the basis of physical arguments, limiting the scope of its applicability [26]. For instance, simultaneous finite support in both domains is mathematically impossible. A measure of effective support can then be constructed by, for example, considering that most of the pulse's energy is contained within the pulse over a finite period of time [24].

The Short-Time Fourier Transform, also known as the spectrogram, is a widely used time-frequency distribution, in fields as diverse as acoustics, seismology and ultra-fast optics. Considering a musical piece where all distinct frequencies easily identify an instrument, a FT of the temporal representation of the musical piece identifies which instruments were played but not when they were played. Gating out the temporal representation of the musical piece using another signal with a finite temporal width and then calculating the former's FT allows for a narrowing down of the temporal presence of each instrument. This is the idea that underpins the spectrogram, which is mathematically represented as:

$$I_{\text{sig}}(\omega, \tau) = \left| \int \mathrm{dt}\ E(t) g(t - \tau)\, \mathrm{e}^{i\omega t} \right|^2, \tag{2.18}$$

where $g(t-\tau)$ is the gating function, centred around the time of interest τ. The spectrogram is given by equation (2.18) for all times of interest.

2.2 Propagation in a Single-Mode Optical Fibre

In defining the analytic representation of an ultrashort pulse the latter was conveniently considered at the origin of the spatial coordinate. However, an ultrashort pulse is always created in a medium (or media) so any phase structure it may have is a consequence of its interaction with that medium. Modelling the light-matter interaction is the necessary first step in a spatial description of the pulse. The common approach is based on classical electromagnetic theory [28]. Recalling the constitutive equations of electromagnetism,

$$\vec{\mathscr{D}} = \varepsilon_0 \vec{\mathscr{E}} + \vec{\mathscr{P}}, \tag{2.19a}$$

$$\vec{\mathscr{B}} = \mu_0 \vec{\mathscr{H}} + \vec{\mathscr{M}}, \tag{2.19b}$$

where $\vec{\mathscr{P}}$ is the electric polarization, i.e. the average number of dipole moments induced by $\vec{\mathscr{E}}$ acting on microscopic bound charges present in a given volume, and $\vec{\mathscr{M}}$ is the magnetic polarization , i.e. the density of permanent or induced magnetic dipole moments in the same volume. Equations (2.19a) and (2.19b) define the electric displacement current and the magnetic flux density, accounting for both free and bound charges. Maxwell's equations describe the relations between the quantities defined in the constitutive equations as follows,

$$\nabla \times \vec{\mathscr{E}} = -\,\partial_t \vec{\mathscr{B}}, \tag{2.20a}$$

$$\nabla \times \vec{\mathscr{H}} = \vec{\mathscr{J}}_{\text{free}} + \partial_t \vec{\mathscr{D}}, \tag{2.20b}$$

$$\nabla \cdot \vec{\mathscr{D}} = \rho_{\text{free}}, \tag{2.20c}$$

$$\nabla \cdot \vec{\mathscr{B}} = 0, \tag{2.20d}$$

where $\vec{\mathscr{J}}_{\text{free}}$ and ρ_{free} are the current density and the charge density of unbound charges respectively. Assumptions about the medium itself help further simplify the problem. Considering a non-magnetic medium without free charges reduces the problem to the extent where it can be solved by relating the electric polarization density with the electric field.

2.2.1 Medium Response

The analysis of a medium's response to $\vec{\mathscr{E}}$ can be performed using a mechanical analogy. Under the harmonic action of $\vec{\mathscr{E}}$ the bound charges oscillate harmonically, and, for sufficiently large $\left|\vec{\mathscr{E}}\right|$, anharmonically. Solving the harmonic case for the position of the bound charge, defines the electric susceptibility χ_{L}, such that

$$\vec{\mathscr{P}}_{\text{L}}(\vec{r},\omega) = \varepsilon_0 \chi_{\text{L}}(\Omega,\omega)\, \vec{\mathscr{E}}(\vec{r},\omega), \tag{2.21}$$

where the subscript L denotes the linear dependence between $\vec{\mathscr{P}}$ and $\vec{\mathscr{E}}$, ω is the driving frequency and Ω is the resonance frequency [28]. In this mechanical analogy it is also possible to calculate susceptibilities for anharmonic oscillations, by expressing $\vec{\mathscr{P}}_{\mathrm{NL}}$ as a perturbation to $\vec{\mathscr{P}}_{\mathrm{L}}$

$$\vec{\mathscr{P}} = \vec{\mathscr{P}}_{\mathrm{L}} + \vec{\mathscr{P}}_{\mathrm{NL}} \tag{2.22}$$

where $\vec{\mathscr{P}}_{\mathrm{NL}} = \vec{\mathscr{P}}^{(2)} + \vec{\mathscr{P}}^{(3)} + \cdots + \vec{\mathscr{P}}^{(n)}$ and $\vec{\mathscr{P}}_{\mathrm{L}} = \vec{\mathscr{P}}^{(1)}$. This is a valid approach provided $|\,\vec{\mathscr{P}}_{\mathrm{NL}}\,| \ll |\,\vec{\mathscr{P}}_{\mathrm{L}}\,|$.

The relative permittivity of a medium ε_r quantifies the medium's resistance to forming electric fields in response to applied electric fields, relative to the vacuum's permittivity, $\varepsilon/\varepsilon_0 = \varepsilon_r$. Given that $\varepsilon_r = 1 + \chi_L$, it follows that the relative permittivity is also frequency dependant, and

$$\vec{\mathscr{D}} = \varepsilon(\omega)\,\vec{\mathscr{E}} + \vec{\mathscr{P}}_{NL}\,. \tag{2.23}$$

Although it is possible to derive explicit formulae for $\vec{\mathscr{P}}$ using the formalism of quantum mechanics [28, p.56-121] the common approach is one based on the above mechanical analogy, providing an adequate description of pulse propagation in fibre-optics, at frequencies far from material resonances [29].

For simplicity only the local response of the medium to $\vec{\mathscr{E}}$ is considered, i.e. spatial dispersion is ignored and the $\vec{r}$ dependence is dropped from equation (2.21). This is justified for wavelengths which are much larger than the typical length of an electric dipole [28, p.34].

The convolution theorem states that $\mathscr{F}\{f\} \cdot \mathscr{F}\{g\} = \mathscr{F}\{f * g\}$, or, equivalently, $\mathscr{F}^{-1}\{\mathscr{F}\{f\} \cdot \mathscr{F}\{g\}\} = f * g$. Keeping with the convention whereby $\vec{\mathscr{P}}^{(1)}(t) = \mathscr{F}^{-1}\left\{\vec{\mathscr{P}}^{(1)}(\omega)\right\}$, and by comparison with equation (2.21), a material response function $R^{(1)}(t-\tau_1)$ can be defined such that

$$\vec{\mathscr{P}}^{(1)}(t) = \varepsilon_0 \int \mathrm{d}\tau_1\, R^{(1)}(t-\tau_1)\,\vec{\mathscr{E}}(\tau_1) = \varepsilon_0 \int \mathrm{d}\tau_1\, R^{(1)}(\tau_1)\,\vec{\mathscr{E}}(t-\tau_1). \tag{2.24}$$

implying that, in general, a material may not polarize instantly. It is also noted that in order to ensure causality, i.e. so that the material does not respond to a field $\vec{\mathscr{E}}(\tau_1)$ that has yet to be applied, $R^{(1)}(t-\tau_1) = 0$ for $\tau_1 < 0$. Equation (2.24) can be generalised for higher order response tensors, yielding

$$\vec{\mathscr{P}}^{(n)}(t) = \varepsilon_0 \int \mathrm{d}\tau_1 \cdots \int \mathrm{d}\tau_n\, R^{(n)}(t-\tau_1,\cdots,t-\tau_n)|\,\vec{\mathscr{E}}(\tau_1)\cdots\vec{\mathscr{E}}(\tau_n), \tag{2.25}$$

where $|$ represents the n^{th} order tensor contraction, normally represented by n vertical dots [28, p.13-17]. The susceptibility is generalised by applying an IFT to the electric fields in equation (2.25) so that the latter becomes,

$$\vec{\mathscr{P}}^{(n)}(t) = \varepsilon_0 \int \mathrm{d}\omega_1 \cdots \int \mathrm{d}\omega_n\, \chi^{(n)}(-\omega_\sigma;\omega_1,\cdots,\omega_n)|\,\vec{\mathscr{E}}(\omega_1)\cdots\vec{\mathscr{E}}(\omega_n)\,\mathrm{e}^{-i\omega_\sigma}, \tag{2.26}$$

where $\omega_\sigma = \omega_1 + \cdots + \omega_n$, such that

$$\chi^{(n)}(-\omega_\sigma;\omega_1,\cdots,\omega_n) = \int \mathrm{d}\tau_1 \cdots \int \mathrm{d}\tau_n (2\pi)^{-n} R^{(n)}(t-\tau_1,\cdots,t-\tau_n)\, \mathrm{e}^{\,i\sum_{j=1}^{n}\omega_j\tau_j}. \tag{2.27}$$

The output from a laser source is not monochromatic, so the quasi-monochromatic approximation it employed, where the field is written as a quasi-monochromatic wave about a characteristic frequency ω', such that

$$\vec{\mathscr{E}}(\omega-\omega') = \frac{1}{2}\left(\vec{E}(\omega-\omega') + \vec{E}^*(-\omega+\omega')\right), \tag{2.28a}$$

or, in the time domain,

$$\vec{\mathscr{E}}(t) = \frac{1}{2}\left(\vec{E}_{\omega'}(t)\,\mathrm{e}^{-i\omega' t} + \vec{E}^*_{\omega'}(t)\,\mathrm{e}^{i\omega' t}\right). \tag{2.28b}$$

In the adiabatic limit, where the response function is effectively instantaneous compared with variations in the pulse's amplitude, and employing the quasi-monochromatic field approximation

$$\vec{P}^{(n)}_{\omega_\sigma}(t) = \varepsilon_0 K(-\omega_\sigma;\omega_1,\cdots,\omega_n)\chi^{(n)}(-\omega_\sigma;\omega_1,\cdots,\omega_n)|\vec{E}_{\omega_1}(t)\cdots\vec{E}_{-\omega_n}(t), \tag{2.29}$$

can be obtained from equation (2.25) [28]. As $\vec{\mathscr{P}}(t)$ and $\vec{\mathscr{E}}(t)$ are both real it follows that $\vec{E}_{\omega'}(t) = \vec{E}^*_{-\omega'}(t)$ and $\vec{P}^{(n)}_{\omega_\sigma}(t) = \left[\vec{P}^{(n)}_{-\omega_\sigma}(t)\right]^*$, where $\vec{P}^{(n)}_{\omega_\sigma}(t)$ follows from writing $\vec{\mathscr{P}}(t)$ in a form similar to $\vec{\mathscr{E}}(t)$ in equation (2.28b), taken at a frequency ω_σ. Thus, only $\frac{1}{2}\vec{E}_{\omega'}(t)\,\mathrm{e}^{i\omega' t}$ and $\frac{1}{2}\vec{P}^{(n)}_{\omega_\sigma}(t)$ were inserted into equation (2.27) in deriving (2.29). The factor $K(-\omega_\sigma;\omega_1,\cdots,\omega_n)$ accounts for these factors of $\frac{1}{2}$ such that $K(-\omega_\sigma;\omega_1,\cdots,\omega_n) \propto 2^{-n+1}$. The factor $K(-\omega_\sigma;\omega_1,\cdots,\omega_n)$ also accounts for the intrinsic permutation symmetry property of the tensor $\chi^{(n)}_{\mu\alpha_1\cdots\alpha_n}(-\omega_\sigma;\omega_1,\cdots,\omega_n)$, where the latter remains invariant under the exchange of the pairs (α_1,ω_1) and (α_2,ω_2), so the former is written $K(-\omega_\sigma;\omega_1,\cdots,\omega_n) = 2^{-n+1}p$ where p is the number of distinct permutations of $\omega_1,\cdots,\omega_n$ [28, p.23-25,122].

Amorphous silica has inversion symmetry so all $\chi^{(2n)}$ are null. The first nonzero nonlinear susceptibility tensor is $\chi^{(3)}$. From the analysis of the symmetry properties of the tensor in an isotropic medium, such as silica, as described by the tensor elements $\chi^{(3)}_{\mu\alpha_1\alpha_2\alpha_3}$ (where μ,α_1,α_2 and α_3 can each run over the cartesian coordinates x, y and z), it follows that only 21 of its 81 components are non-zero, and of those only 3 are linearly independent. In particular [28, p.302],

$$\chi^{(3)}_{xxxx} = \chi^{(3)}_{xxyy} + \chi^{(3)}_{xyxy} + \chi^{(3)}_{xyyx} \tag{2.30a}$$

and

$$\chi^{(3)}_{xxxx} = \chi^{(3)}_{yyyy} = \chi^{(3)}_{zzzz} \tag{2.30b}$$

Far from transition frequencies of the material, e.g. where the material is mostly transparent to the optical radiation travelling through it, the Kleinman Symmetry is valid, so the frequencies $\omega_1,\cdots,\omega_n$ can be exchanged without exchanging their respective indices $\alpha_1,\cdots,\alpha_n$, e.g. $\chi^{(n)}_{\mu\alpha_1\cdots\alpha_n}(-\omega_\sigma;\omega_1,\cdots,\omega_n) = \chi^{(n)}_{\mu\alpha_1\cdots\alpha_n}(-\omega_\sigma;\omega_n,\cdots,\omega_1)$ [28, p.123].

For $n = 3$, $\omega_1 = \omega_0$ and $\omega_3 = -\omega_2 = \omega_0$, equation (2.29) becomes,

$$P^{(3)}_{\mu,\omega_0}(t) = \frac{3\varepsilon_0}{4}\chi^{(3)}_{\mu\alpha_1\alpha_2\alpha_3}E^{\omega_0}_{\alpha_1}(t)E^{-\omega_0}_{\alpha_2}(t)E^{\omega_0}_{\alpha_3}(t), \tag{2.31}$$

employing the Einstein summation convention. This choice of frequencies results in a tensor which describes nonlinear phenomena which result from an intensity dependant change in refractive index [28]. Applying the intrinsic permutation symmetry, the spatial symmetry and the Kleinman symmetry to (2.31), as well considering any field contributions along $\hat{z}$ are null, it can be written that

$$P^{(3)}_{x,\omega_0}(t) = \frac{3\varepsilon_0}{4}\chi^{(3)}_{xxxx}\left[\left(\left|E^{\omega_0}_x(t)\right|^2 + \frac{2}{3}\left|E^{\omega_0}_y(t)\right|^2\right)E^{\omega_0}_x(t) + \frac{1}{3}E^{-\omega_0}_x(t)E^{\omega_0}_y(t)E^{\omega_0}_y(t)\right] \tag{2.32}$$

with a similar expression for $P^{(3)}_{y,\omega_0}(t)$ given by swapping x and y in the equation above.

2.2.2 Fundamental Mode

Replacing equations (2.19b) and (2.23) in (2.20b), taking the partial derivative in respect to time and replacing $\partial_t\vec{B}$ with $-\nabla\times\vec{\mathscr{E}}$ (cf. equation (2.20a)) yields

$$\nabla\times\nabla\times\vec{E}(t) + \mu_0\varepsilon(\omega)\,\partial_t^2\,\vec{E}(t) = -\mu_0\,\partial_t^2\,\vec{P}_{\mathrm{NL}}(t), \tag{2.33}$$

and, by applying a FT to (2.33),

$$\nabla\times\nabla\times\vec{E}(\omega) - \mu_0\omega^2\varepsilon(\omega)\vec{E}(\omega) = \mu_0\omega^2\vec{P}_{NL}(\omega), \tag{2.34}$$

where the complex conjugates of these equations were simply omitted as they contain equivalent information.

In its simplest form an optical fibre is a waveguide, composed by two concentric cylindrical layers, the core with radius a and refractive index n_1, and the cladding, with radius b and refractive index n_2. Due to the perturbative nature of $\vec{P}_{\mathrm{NL}}$ the latter is omitted from the equation, yielding the Helmoltz Equation,

$$\nabla^2\vec{E}(\omega) + k^2\varepsilon_r(\omega)\vec{E}(\omega) = 0, \tag{2.35}$$

where the vector identity $\nabla\times\nabla\times\vec{\mathscr{E}} = \nabla(\nabla\cdot\vec{\mathscr{E}}) - \nabla^2\vec{\mathscr{E}}$ was applied using equation (2.23) in the frequency domain, and $\mu_0\omega^2\varepsilon(\omega) = k^2\varepsilon_r(\omega)$ since $\mu_0\varepsilon_0 = c^{-2}$ and $\varepsilon_r(\omega) = n^2(\omega) \equiv c^2/c^2_{\mathrm{medium}}$. In general, equation (2.35) is solved in cylindrical polar coordinates, by separation of variables, and takes into account all 6 possible components of the electromagnetic field inside the fibre. In doing so, a normalised frequency $V = ka\sqrt{n_1^2 - n_2^2}$ is defined, such that for $V < 2.405$ only a single mode is allowed in the fibre. This mode, the fundamental mode, is doubly-degenerate, equivalent to having one linearly polarized mode along $\hat{x}$ and another along $\hat{y}$, with the same profile $F(x, y)$ [29, 30], so that

$$E_\mu(\vec{r}, \omega - \omega_0) = F(x, y)A_\mu(z, \omega - \omega_0)\,\mathrm{e}^{i\beta_{0\mu}z}, \tag{2.36a}$$

or, in the time-domain,

$$E_\mu(\vec{r},t) = F(x,y)A_\mu(z,t)\,\mathrm{e}^{i(\beta_{0\mu}z-\omega_0 t)}\,. \tag{2.36b}$$

The propagation constant $\beta_{0\mu}$ should in principle be equal for both polarizations, denoted by the index μ. However, an optical fibre's symmetry may vary over its length, due to mechanical stresses, or the fibre may even have asymmetries acquired during manufacturing, causing birefringence, which may even be purposefully engineered [29].

2.2.3 Propagation Equation in the Frequency Domain and Dispersion

Replacing the fundamental mode into the Helmholtz equation yields two equations, by separation of variables, one longitudinal and one cross-sectional. Solving the latter leads to solutions for the separation variable, $\beta(\omega)$, which accounts for waveguide dispersion. The longitudinal and cross-sectional equations are

$$\left(\partial_x^2+\partial_y^2\right)F(x,y)+\left(\varepsilon_{r\mu}(\omega)k^2-\beta^2(\omega)\right)F(x,y)=0, \tag{2.37a}$$

and

$$\left[2i\beta_{0\mu}\partial_z+(\beta_\mu^2(\omega)-\beta_{0\mu}^2)\right]A_\mu(z,\omega-\omega_0)=0, \tag{2.37b}$$

respectively, where the slowly varying envelope approximation was applied in writing the first term on the left-hand side of equation (2.37b). This is the starting point for describing propagation of the fundamental mode in an optical fibre.

Dispersion is accounted for by expanding $\beta_\mu(\omega)$ about the carrier frequency ω_0, so that

$$\beta_\mu(\omega)=\beta_{0\mu}+\beta_{1\mu}(\omega-\omega_0)+\frac{1}{2}\beta_2(\omega-\omega_0)^2+\frac{1}{6}\beta_3(\omega-\omega_0)^3+\cdots, \tag{2.38}$$

where $\beta_m=\frac{d^m\beta}{d\omega^m}\big|_{\omega=\omega_0}$ for all $m\in[1,\infty[$. As it can be shown that $\beta_{1\mu}=1/v_{g\mu}$ which is why the latter is taken as the highest order term in $\beta_\mu(\omega)$ describing birefringence in the fibre [29]. The delay experienced by the amplitude, cf. equation (2.12), is related to its group velocity v_g, which effectively links the dispersive action of the medium, via $\beta_{1\mu}$ to the information contained in $\Phi_0^{(1)}$. Similarly, the information provided by $\Phi_0^{(2)}$, can be linked to the dispersive effects quantised by β_2. Specifically, equation (2.14) shows there is a frequency dependence to the group delay, implying there is group delay dispersion (GDD). Defining the dispersion parameter such that $D\equiv\frac{d}{d\lambda}\beta_1$, by noting that $\beta_2=\frac{d\beta_1}{d\omega}$, and given that $\frac{d}{d\omega}=\frac{d\lambda}{d\omega}\frac{d}{d\lambda}$, it follows that $D=-\frac{2\pi c}{\lambda^2}\beta_2$. Comparing these two expressions for D readily reveals an underlying physical mechanism quantised by β_2, the group velocity is affected by dispersion (GVD) leading to broadening or compression of the envelope. It is conventional to denote the chromatic dispersion as anomalous when $D>0$, i.e. when the GV decreases with λ, and normal when $D<0$, i.e. when the GV increases with λ.

Making the transformation of variables $\omega-\omega_0\to u$, and replacing all powers of u in equation (2.38) with the frequency operator (cf. equation (2.8a) yields,

$$\beta_\mu(\omega)\to\beta_{0\mu}+i\beta_{1\mu}\partial_t-\frac{1}{2}\beta_2\partial_t^2-\frac{i}{6}\beta_3\partial_t^3+\cdots. \tag{2.39}$$

2.2.4 Propagation Equation in the Time Domain and Nonlinear Effects

The nonlinear term which was omitted from equation (2.35) is accounted for by a perturbation to $\varepsilon(\omega)$, such that

$$\varepsilon_{r\mu}(\omega) = n_\mu^2 \rightarrow (n_\mu + \Delta n_\mu)^2 \approx n_\mu^2 + 2n_\mu \Delta n_\mu, \tag{2.40}$$

where Δn_μ accounts for the change in the refractive index along $\hat{\square}$ due to nonlinear effects, and also takes fibre losses into account (as n is complex in general). The perturbation term is written so that an expression for the total polarization can be written in a fashion similar to that for the linear polarization (cf. equation (2.21)), such that P_{x,ω_0} is related to $E_x^{\omega_0}$ by an effective susceptibility tensor. Thus, using equation 2.32 the perturbative term can be written

$$\Delta n_x = \frac{3}{8n_\mu}\chi^{(3)}_{xxxx}\left[\left|E_x^{\omega_0}(t)\right|^2 + \frac{2}{3}\left|E_y^{\omega_0}(t)\right|^2 + \frac{1}{3}E_y^{-\omega_0}(t)E_y^{-\omega_0}(t)\right] + i\frac{\alpha}{2k}, \tag{2.41}$$

and similar expressions can be written for Δn_y and $E_y^{\omega_0}(t)$, Δn_y^* and $E_y^{-\omega_0}(t)$, and Δn_x^* and $E_x^{-\omega_0}(t)$. The change in refractive index along $\hat{\mathbf{x}}$ depends on both $E_x^{\omega_0}(t)$ and $E_y^{\omega_0}(t)$. The nonlinear effect described by $E_x^{\omega_0}(t)$ is called self-phase modulation (SPM) as the phase of a pulse travelling in the medium will be altered due to the change in refractive index caused by itself. The nonlinear effect described by $E_y^{\omega_0}(t)$ is called cross-phase modulation (XPM) as the phase of a pulse travelling in the medium will be altered due to the change in refractive index caused by the co-propagating pulse. From (2.41) a measure of the medium's non-linearity, n_2 is normally defined such that,

$$n_2 = \frac{3}{8n}\chi^{(3)}_{xxxx}. \tag{2.42}$$

Equation (2.37b) can be further simplified by approximating $\beta_\mu^2(\omega) - \beta_{0\mu}^2(\omega)$ as $2\beta_{0\mu}(\omega)(\beta_\mu(\omega) - \beta_{0\mu}(\omega))$. Before taking into account the effect of dispersion, it can be noted that the change in refractive index which accounts for the non-linearities will alter the value of the propagation constant given by equation (2.37a). This change is accounted for by a first order perturbation [29] such that $\beta_\mu(\omega) \rightarrow \beta_\mu(\omega) + \Delta\beta_\mu$, where

$$\Delta\beta_\mu = \frac{n_\mu(\omega)k^2}{\beta_\mu(\omega)}\frac{\iint \mathrm{dx\,dy}\,\Delta n_\mu \left|F(x,y)\right|^2}{\iint \mathrm{dx\,dy}\left|F(x,y)\right|^2}. \tag{2.43}$$

By including this perturbation in the simplified version of equation (2.37b), applying an IFT to it, including dispersion to second order and defining an effective mode area $A_{\mathrm{eff}} = \left(\iint \mathrm{dx\,dy}\left|F(x,y)\right|^2\right)^2 / \iint \mathrm{dx\,dy}\left|F(x,y)\right|^4$, two coupled mode equations can be written in the time domain [29],

$$\partial_z A_x + \beta_{1x}\partial_t A_x + \frac{i\beta_2}{2}\partial_t^2 A_x + \frac{\alpha}{2}A_x = i\gamma\left(\left|A_x\right|^2 + \frac{2}{3}\left|A_y\right|^2\right)A_x + \frac{i\gamma}{3}A_x^* A_y^2\,\mathrm{e}^{-2i\Delta\beta' z}, \tag{2.44a}$$

and

$$\partial_z A_y + \beta_{1y}\partial_t A_y + \frac{i\beta_2}{2}\partial_t^2 A_y + \frac{\alpha}{2}A_y = i\gamma\left(\left|A_y\right|^2 + \frac{2}{3}\left|A_x\right|^2\right)A_y + \frac{i\gamma}{3}A_y^* A_x^2\,\mathrm{e}^{2i\Delta\beta' z}. \tag{2.44b}$$

In writing the equations above the nonlinear parameter γ was defined such that

$$\gamma = \frac{n_2' \omega_0}{c A_{\text{eff}}}, \tag{2.45}$$

where A_x and A_y have been normalised so that $\left|A_x\right|^2$ and $\left|A_y\right|^2$ are in units of power. The parameter $\Delta\beta' = \beta_{0y} - \beta_{0x} = 2\pi/L_B$ accounts for modal birefringence. If $L_B \ll L$, where L is the length of the fibre, when the fibre is highly birefringent or the fibre is very long, then the last term in equation (2.44a) can be discarded. Over short lengths of low birefringence fibres the term becomes more significant [29].

Two other useful characteristic lengths are the dispersive length $L_D^{(n)} = T^n / \left|\beta_n\right|$ and the nonlinear length L_{NL}=1/(γP_{peak}), where P_{peak} is the pulse's peak power. The ratio between these two characteristic lengths provides some intuition about whether dispersion or nonlinearities will dominate the propagation of a pulse over a length of fibre [29].

Chapter 3

Frequency-Resolved Optical Gating

Frequency-Resolved Optical Gating (FROG) was invented by Trebino et al. [15] as a means of characterising an arbitrary ultra-short pulse, i.e. retrieving its phase and amplitude. The success of this technique lies in its ability to address two fundamental issues in ultra-short pulse characterization. Direct measurements in time require events smaller than the measured event in order to resolve the latter. Direct measurements of ultra-short light pulses are thus limited to the spectral domain. Secondly, the spectrum of a pulse does not provide enough information for characterising the pulse: any direct measurements of the pulse yield only its spectrum, never its phase.

The fundamental theorem of algebra implies that any attempt at retrieving the phase of an ultra-short pulse from a univariate discrete data set is effectively impossible. If the set corresponding to a measured spectrum is $\left\{\left|F_k\right| : k \in [1, N]\right\}$ then the set that must be determined is $\left\{f_m : m \in [1, N]\right\}$, and they are related by a DFT,

$$F_k = \sum_{m=1}^{N} f_m \, \mathrm{e}^{i2\pi mk/N} = \sum_{m=1}^{N} f_m z^m. \tag{3.1}$$

In the form presented in equation (3.1), the DFT F_k is a univariate polynomial in the complex variable z. It can thus be factorised such that $F_k = f_N(z - z_1)(z - z_2)\cdots(z - z_N)$. Given that what is measured in the laboratory is $\left|F_k\right| = \left|f_N(z - z_1)(z - z_2)\cdots(z - z_N)\right|$ there are ambiguities in the phase associated with $\left|F_k\right|$ as the complex-conjugation of the N factors leaves $\left|F_k\right|$ unaltered. Pulses with many different phases can have the same intensity, or, simply, the magnitude of a complex number contains no phase information.

The point of interest regarding the fundamental theorem of algebra is it is only valid for polynomials of one variable. This does not mean all polynomials of two or more variables cannot be factored, but doing so becomes harder as N increases. Considering a two-dimensional discrete data-set $\left\{\left|F_{k,h}\right| : k, h \in [1, N]\right\}$, e.g. that resulting from a spectrogram, the two-dimensional DFT can be written,

$$F_{k,h} = \sum_{m,n=1}^{N} f_{m,n} \, \mathrm{e}^{i2\pi(-mk+nh)/N} = \sum_{m,n=1}^{N} f_{m,n} z^m y^n. \tag{3.2}$$

If N is sufficiently large that $F_{k,h}$ cannot be factored then only three ambiguities exist in $\left|F_{k,h}\right|$:

1. an absolute phase factor, $\left|F_{k,h}\,\mathrm{e}^{(-i\phi_0)}\right| = \left|F_{k,h}\right|$;

2. a translation $\left|F_{k-k',h-h'}\right| = \left|F_{k,h}\right|$;

3. a time-reversal $\left|F^*_{-k,-h}\right| = \left|F_{k,h}\right|$.

Recalling the absolute phase term from §2.1.1 it can be seen that if the pulse's carrier frequency is large the carrier is well represented by the amplitude, so the constant phase can be ignored for a particular reference time. The first order phase results in a translation which is ignored since it leaves the amplitude and the phase unchanged. A time reversal corresponds to the transformation $t \to -t$ and a change of sign in the phase, so it is also considered a trivial ambiguity [14]. FROG is thus cast as a two-dimensional phase retrieval problem [15].

Experimentally producing such a discrete data set involves a slight modification of the spectrogram (cf. (2.18)), where $E(t)g(t-\tau)$ is replaced by $E_{\text{sig}}(t,\tau)$, resulting from the gating of the pulse $E(t)$ by a delayed replica $E(t-\tau)$, in an instantaneously responding non-linear medium, yielding what is known as the FROG trace,

$$I_{\text{FROG}}(\omega,\tau) = \left| \int \mathrm{dt}\; E_{\text{sig}}(t,\tau)\, \mathrm{e}^{i\omega t} \right|^2 . \tag{3.3}$$

At first sight this is just another one-dimensional phase-retrieval problem, yet $E_{\text{sig}}(t,\tau)$ can be seen as the one-dimensional IFT of $E_{\text{sig}}(t,\Omega)$ such that

$$I_{\text{FROG}}(\omega,\tau) = \left| \frac{1}{2\pi} \int \int \mathrm{dt}\, \mathrm{d}\Omega\; E_{\text{sig}}(t,\Omega)\, \mathrm{e}^{i(\omega t - \Omega\tau)} \right|^2 . \tag{3.4}$$

Determining $E_{\text{sig}}(t,\Omega)$, or equivalently, $E_{\text{sig}}(t,\tau)$ and setting $\tau = t$ determines $E(t)$ for any $E_{\text{sig}}(t,\tau = t) \propto E(t)$, given that the aim is to know the shape of $E(t)$ and not necessarily its absolute value (which explains why proportionality constants were ignored in stating equation (2.2)).

Generating I_{FROG} from E_{sig} is simply taking an intensity autocorrelation and resolving it in frequency [14, pp. 61-99]. The FROG geometry defines the variant of the technique depending on the nonlinear material, the experimental setup or by the nonlinearity which is exploited, for example:

Table 3.1: Two FROG geometries. Adapted from [16].

Geometry	Nonlinearity	$E_{\text{sig}}(t,\tau)$
Second Harmonic Generation (SHG)	$\chi^{(2)}$	$\propto E(t)E(t-\tau)$
Polarization Gating (PG)	$\chi^{(3)}$	$\propto E(t)\left\|E(t-\tau)\right\|^2$

3.1 Fibre-FROG

By defining right and left circularly polarized states, $A_+ = (A_x\, \mathrm{e}^{i\Delta\beta z/2} + iA_y\, \mathrm{e}^{-i\Delta\beta z/2})/\sqrt{2}$ and $A_- = (A_x\, \mathrm{e}^{i\Delta\beta z/2} - iA_y\, \mathrm{e}^{-i\Delta\beta z/2})/\sqrt{2}$ respectively, equations (2.44a) and (2.44b) can be re-written

$$\partial_z A_+ + \beta_{1x}\partial_t A_+ + \frac{i\beta_2}{2}\partial_t^2 A_+ + \frac{\alpha}{2}A_+ = \frac{i2\gamma}{3}\left(\left|A_+\right|^2 + 2\left|A_-\right|^2\right)A_+ + \frac{i}{2}\Delta\beta A_-, \tag{3.5a}$$

and

$$\partial_z A_- + \beta_{1y}\partial_t A_- + \frac{i\beta_2}{2}\partial_t^2 A_- + \frac{\alpha}{2}A_- = \frac{i2\gamma}{3}\left(\left|A_-\right|^2 + 2\left|A_+\right|^2\right)A_- + \frac{i}{2}\Delta\beta A_+. \tag{3.5b}$$

Noting that in this form the effect of XPM is two times stronger than the effect of SPM, compared to two thirds stronger in equations (2.44a) and (2.44b), Thomson et al. [8] proposed the fibre-FROG geometry. In the absence of dispersion, power losses, and for negligible birefringence (3.5a) is written

$$\partial_z A_+ = \frac{2i\gamma}{3}\left(\left|A_+\right|^2 + 2\left|A_-\right|^2\right)A_+. \tag{3.6}$$

From the equation above it can be shown that the output signal from a fibre of length L resulting from an input of two oppositely circularly polarized fields, $E(t) = A_+(t, z = 0)$ and $E(t-\tau) = A_-(t, z = 0)$, is [8, 29]

$$E_{\text{sig}}^{\text{fibre-FROG}}(t,\tau) = E(t)\,\mathrm{e}^{\frac{i2\gamma L}{3}(|E(t)|^2+2|E(t-\tau)|^2)}. \tag{3.7}$$

Obtaining $E_{\text{sig}}^{\text{fibre-FROG}}$ is then a matter of creating $E(t)$ and $E(t-\tau)$ from the input pulse which needs to be characterised. This is achieved using a Michelson interferometre, cf. figure 3.1.

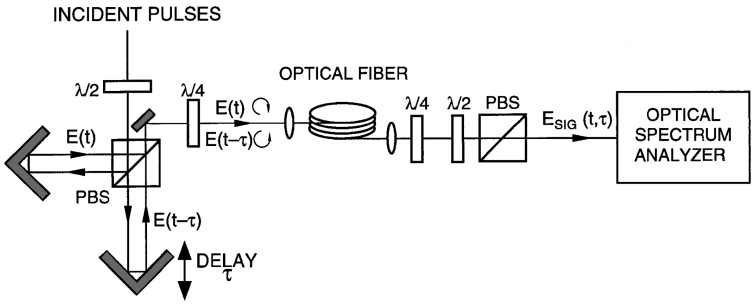

Figure 3.1: fiber-FROG experimental setup. Adapted from [8]

The first half-wave plate ($\lambda/2$) in figure 3.1 is used to adjust the linear state of the incoming pulse so that the power is split evenly among both branches of the interferometre by the polarization beam-splitter (PBS). The static branch is travelled by $E(t)$ and the adjustable branch by $E(t-\tau)$. Once $E(t)$ and $E(t-\tau)$ travel through the interferometre and become collinear, they are both reflected into a quarter-wave plate ($\lambda/4$), becoming right and left circularly polarised respectively. Once the circularly polarised modes have been inserted into the fibre, and propagate through it, the output is filtered in respect to $E(t)$: a quarter-wave plate converts the circular modes back to linear modes and a half-wave plate and a polarising beam splitter are used in combination to select $E_{\text{sig}}^{\text{fibre-FROG}}(t,\tau)$, which is measured by a spectrometer.

3.2 Limits on Acquiring and Simulating Data

Considering a pulse in the time domain, as represented by a set of N discrete points separated by a step Δt it follows that

$$\Delta t(N-1) = t_{\text{range}} \tag{3.8}$$

where $t_{\text{range}} = t_{\text{f}} - t_{\text{i}}$ is the set's range, t_{f} and t_{i} are the last and first points in the set respectively.
Understanding the limits on data sampling in FROG is not straightforward, as a pulse does not have true finite support in time, e.g. a gaussian pulse is only 0 in the limit of infinite time, in both the past and the future. This motivates considering $t_{\text{range}} = bT$, where b is a constant and T is the rms temporal width of measured pulse. For example, 99.9999% of a Gaussian pulse's energy is contained within t_{range} if $b = 5$. This is reasonable physical argument for considering the pulse is effectively time-limited, in the sense that it has an effective temporal duration.
In constructing the spectrogram the delay step $\Delta\tau$ is only limited by the path length difference generated along the adjustable branch of the interferometre, and the speed of light in air, from which it follows that

$$\Delta\tau = \frac{2\Delta s}{c}, \tag{3.9}$$

where $2\Delta s$ is the total difference in path length resulting from the change in position Δs along the adjustable branch of the interferometre. Physically, $\Delta\tau$ is only limited by the translation stage, e.g. a translation stage capable of producing a minimum $\Delta s = 0.3\,\mu\text{m}$ can produce a temporal resolution of $\Delta\tau = 2\,\text{fs}$ at best. It is also completely independent from, yet considered equal to, Δt. This choice simplifies the coding of the reconstruction algorithm in dealing with terms of the form $E(t - \tau)$.
Another practical consideration concerning the reconstruction algorithm involves the restriction on the number of data points representing $E(t)$ and hence $E_{\text{sig}}(t, \tau)$. The former must be transformed between the time and spectral domains over the course of the reconstruction algorithm, and these conversions are performed by FFT routines which are optimised for sets containing $N = 2^n$ points where $n \in \mathbb{N}$.
While the frequency step Δf is physically limited only by the resolution of the instrument measuring the spectrum, setting $\Delta t = \Delta\tau$ limits Δf, via the FFT, to

$$\Delta f = \frac{1}{N\Delta\tau}, \tag{3.10}$$

which also sets the spectrogram size to $N \times N$. Applying a similar argument to that applied to (3.8), but in the frequency domain, yields

$$\Delta f(N - 1) = dB, \tag{3.11}$$

where d is a constant and B the pulse's bandwidth. Then, multiplying equations (3.8) and (3.11) yields

$$BT = \frac{1}{bd}\left(N - 2 + \frac{1}{N}\right). \tag{3.12}$$

For large N equation (3.12) shows the maximum TBP representable by a FROG trace scales (roughly) with N. The more complex the pulse the bigger the trace required to represent it.
However, the absence of a priori knowledge of the constants b and d in equation (3.12) means the choice of the FROG trace size is an experimental issue. The criterion employed to this end is termed the FSR, where it is assumed the pulse is completely represented by the FROG trace if the intensity of all points along the edges of the trace is less than $10^{-4} I_{\text{FROG}}^{\max}$, where $I_{\text{FROG}}^{\max}$ is the maximum intensity on the FROG trace [31].
To create an experimental trace, a spectrum of $I_{\text{FROG}}(\lambda, \tau)$ is acquired for each value of τ, which must then be interpolated to $I_{\text{FROG}}(\omega = 2\pi f, \tau)$ before the trace can be used with a reconstruction

algorithm. Conversely, the same is valid for a simulated trace if it is to serve as a valid guiding tool for experimental data collection. The point of interest concerning this interpolation, and its impact on the parameters for data collection and simulation, stems from the nonlinear relation between frequency step Δf (ignoring the multiplicative constant 2π for simplicity) and the wavelength step $\Delta\lambda$,

$$\Delta f = \frac{c}{\lambda^2}\Delta\lambda. \tag{3.13}$$

Taking equations (3.9) and (3.10) shows that a constant Δf corresponds to a constant Δs. Although this is convenient for the purpose of implementing the algorithm, as it means Δt is fixed, it does not match the reality of acquiring data as, in an experimental setting, $\Delta\lambda$ is also fixed. However, the number of experimentally obtained points is not limited to N, although the less points are collected the faster the FROG trace can be constructed. More to the point, the arbitrary limit on the number of experimentally acquired data points means that in order to ensure a good interpolation of that data, a simple condition can be imposed on Δf: if λ_{max} is the wavelength corresponding to $I_{\text{FROG}}(\lambda_{\text{max}}, \tau)$, such that $I_{\text{FROG}}(\lambda > \lambda_{\text{max}}, \tau)$ contains no significant amount of energy, as defined by the FSR, then, from equation (3.13), it follows that

$$\Delta f \geq \frac{c}{\lambda_{\text{max}}^2}\Delta\lambda. \tag{3.14}$$

Similarly, the upper bound on Δf can be given by

$$\Delta f \leq \frac{c}{\lambda_{\text{min}}^2}\Delta\lambda, \tag{3.15}$$

where $\lambda = \lambda_{\text{min}}$ is such that $I_{\text{FROG}}(\lambda < \lambda_{\text{min}}, \tau)$ contains no significant amount of energy, as determined by the FSR.

In fibre-FROG the physical parameters which determine λ_{max} and λ_{min} are γ and L as well as T_{FWMH} and P_{peak}. Assuming a gaussian shape for an uncharacterised pulse with $T_{\text{FWMH}} = T\sqrt{2ln(2)} = 100$ fs, and $E_T = 24$ pJ, the peak power (P_{peak}) is 225.5 W. The minimum length for L is set by L_{NL}, which for $\gamma = 2.36\,\text{W}^{-1}\,\text{km}^{-1}$ [32] means $L > 1.88$ m. The upper bound on L is set by L_{D}. For $L_{\text{NL}}/L_{\text{D}} \ll 1$, the nonlinear effects which provide the gating mechanism for FROG should dominate over dispersive effects. From the experimentally collected data (presented in figure 4.9 in §4.2) it is seen that $L_{\text{NL}}/L_{\text{D}} = 0.15$ and that dispersion is significant on the time scale of 100 fs. For theses reasons L is considered equal to 2 m.

If under the above physical parameters, $\lambda_{\text{min}} = 1500$ nm and $\lambda_{\text{max}} = 1600$ nm, and setting $\Delta\lambda = 4.14$ nm, the time step $\Delta t = 14.17$ fs corresponds to the maximum allowed frequency step, as determined by equation (3.15) for $N = 128$. Fixing N sets both t_{range} and f_{range}. Even though this appears like a case of undersampling, as the range between λ_{min} and λ_{max} is approximately equal to only $24 \times \Delta\lambda$, any lack of information in the spectral dimension is compensated by the temporal dimension as long as the FSR is obeyed in both dimensions [14]. A measure of how evenly the information is distributed over the spectral and temporal dimensions of the spectrogram can be defined

using equations (3.9) and (3.11) such that

$$\frac{b}{d} = \frac{B}{TN\Delta f^2}. \tag{3.16}$$

With the limits on Δf imposed by equations (3.14) and (3.15) it is easy to gauge the aspect ratios which are possible for a particular number of points and TBP. This way, simulation parameters can be selected on the basis of a trace's experimentally observed $\lambda_{\min}$ and $\lambda_{\max}$ as well as the minimum $\Delta\lambda$ required to properly resolve all of the features in signal's spectrum, and the pulse's bandwidth. Conversely, limits on $\Delta\lambda$, $\lambda_{\max}$ and $\lambda_{\min}$ can be gauged for a pulse with an assumed TBP, and the desired number of sampling points as well as the desired sampling ratio b/d.

3.3 Reconstruction Algorithm

Performing the 2D Phase Reconstruction in FROG relies on the idea that the a-priori unknown signal $E_{\mathrm{SIG}}(\omega, \tau)$, resulting from the equations that govern the behaviour of the uncharacterised field $E(t)$ in the nonlinear medium, and the square root of the experimentally measured signal field, $\sqrt{I_{\mathrm{SIG}}(\omega, \tau)}$, form two distinct, possibly convex, sets. The aim is to iterate between these two sets, by optimising the alternating projection into either set, until the field $E(t)$ common to both sets is found. This is known as generalised projections (GP) [18, 33].

There is no mathematical guarantee these sets are convex, which as well as potentially causing stagnation of the reconstruction algorithm, also means a field common to both sets may never be found. For this reason, and to monitor convergence of the algorithm, the FROG root mean square, G_{FROG}, is defined as a measure of convergence, such that

$$G_{\mathrm{FROG}} = \frac{1}{N}\sqrt{\sum_{i,l=1}^{N}\left[I_{\mathrm{FROG}}(\omega_i, \tau_l) - I^k_{\mathrm{FROG}}(\omega_i, \tau_l)\right]^2}, \tag{3.17}$$

where k is the current iteration of the GP algorithm [17].

The optimisation is directed using local information regarding the field $E^k(t)$, by minimising a functional distance metric between the two sets in GP in respect to $E^k(t)$ [17, 33]. This produces an analytic derivative expression, specific to the FROG geometry in use, which is used in a steepest descent optimisation.

Despite GP's success in retrieving a vast majority of simulated pulses, for different FROG geometries, and TBPs of up to 100 [34], the algorithm is applicable only if the analytic form of $E_{\mathrm{SIG}}(t, \tau)$ is obtainable from the propagation equation.

3.3.1 Genetic Algorithm

Genetic Algorithms (GAs) are, in a narrow sense, a type of optimisation algorithm [35]. These are often employed where calculus-based approaches are not applicable, e.g. when there is no analytic expression relating the optimised result and the variable(s) upon which the former depends. Additionally, GAs have been used successfully with SHG FROG [19] and to varying degrees of success with

fibre-FROG [21]. For these reasons a GA was developed and used in the course of this thesis. Formally, the aim in any optimisation problem is the optimisation of I parameters, in this case

$$E_i = E(\omega_i) = \sqrt{S(\omega_i)}\, e^{i\Phi(\omega_i)}, \tag{3.18}$$

i.e each component of the spectral amplitude, by minimising an objective function. Restrictions may also apply to each parameter. If $\sqrt{S(\omega_i)}$ is obtained experimentally, and normalised to the pulse's energy,$\Phi_i = \Phi(\omega_i)$ is now the i^{th} optimisation parameter. Choosing the latter's principle-value representation, or wrapped phase, it follows that

$$-\pi \leq \Phi(\omega_i) \leq \pi, \tag{3.19}$$

formally termed an inequality restriction.

Many types of algorithms inspired by natural-selection were created and developed between the 1950s and the 1970s , most notably John Holland's (canonical) GA, which in its basic form optimises the objective function by applying three genetic operators to iterate between generations of a population: Selection, Crossover and Mutation [36].

A population, `pop(i, j)`, is defined as a set of J chromosomes, which are essentially coded strings, originally in binary form, where each individual 0 or 1 is termed a gene.

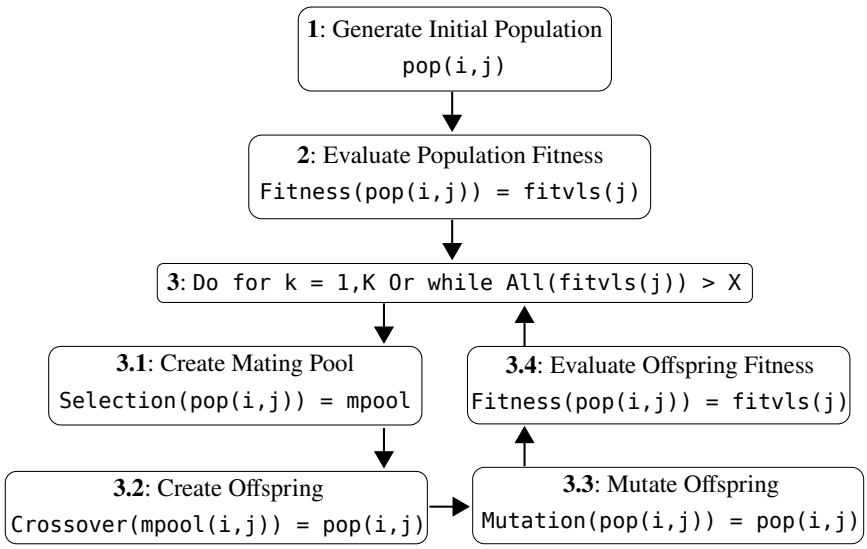

Figure 3.2: GA fluxogram with pseudocode. The indices i, j and k identify the gene, chromosome and generation, and span from 1 to I, 1 to J and 1 to K respectively, in integer steps . The indices q and p identify the gene and chromosome in the mating pool, spanning from 1 to $Q = I$ and 1 to P respectively, in integer steps. The first letter of function names are capitalised and variable names are all lower case.

However, many GA applications have successfully used real-valued genes [37], and efforts have been made to extend GA theory to this encoding [38]. In the current thesis each chromosome was coded as an array of real numbers, such that each gene represents a particular value of the spectral phase, following existing work where GAs were used for FROG pulse reconstruction [19, 21].

Also following the work of Vrany et al. [21] the initial random spectral phase was created by taking randomly generated numbers from a uniform distribution between $-\pi$ and π.
Due to the stochastic nature of all three GA operators the concepts of exploitation and exploration have become central to describing how GAs optimise in the search space [39]. Succinctly, Exploration optimises in entirely new regions of the search space where as Exploitation optimises around known regions. The balance between these two behaviours determines the GAs success in guiding the optimisation, determining, for example, how many iterations are needed for convergence or if premature convergence occurs. Extending the analogy with nature, the ratio between exploitation and exploration can be compared to genetic diversity. If most of the information encoded in each chromosome (by individual genes or groups of genes) is similar among all chromosomes in a population then exploitation dominates and diversity is low. On the other hand, if the population has a large diversity, exploration dominates and the GA looks like a random search. By employing Selection, Crossover and Mutation GAs achieve a balance between Exploitation and Exploration, keeping fit genes or gene sequences and finding fitter ones [36].

Objective Function

Once the initial population has been generated, cf. step 1 in figure 3.2, the fitness values of its J chromosomes are calculated and stored in `fitvls(j)`, cf. step 2 in figure 3.2. Fitness, $f(j)$, is a measure of how good a solution the j^{th} chromosome represents, as gauged by comparing the value calculated by the objective function to a reference value, X.
In this thesis the starting point for the objective function was

$$G_{\text{FROG}}(j), \tag{3.20}$$

as was the case in other related work [19, 21]. Thus, the smaller $G_{\text{FROG}}(j)$ the greater the fitness of the j^{th} chromosome. Depending on the selection method which is employed, and whether maximization or minimization of objective function is desired, the values produced by the latter may not correspond directly to the fitness values.

Selection

Selection in a GA is the process whereby all the chromosomes necessary to generate the mating pool `mpool(q, p)`, i.e. the group of P chromosomes that will be combined to generate offspring in the GA, cf. step 3.1 in figure 3.2. The offspring become the population at iteration $k + 1$ where k is the current GA iteration and runs from 1 to K.
Several Selection operators are used with GAs. Most commonly these rely either on rank (RS), where the fitness values are ranked from the fittest to the least fit and the selection probability (p_{s}) of each chromosome is a function of its rank, or on the fitness value itself, where $p_{\text{s}}(j) \propto f(j)$, termed proportional selection (PS) [40].
Roulette Wheel Selection (RWS) is the most commonly employed PS operator. In RWS, selection is based on mapping the individual fitness values onto the circumference of a roulette wheel, where

chromosomes take up an arc length which is proportional to their fitness value. The wheel is then spun and when it stops a chromosome is selected into the mating pool. The probability of selection is then,

$$p_s(j) = \frac{f(j)}{\sum_{j=1}^{J} f(j)}. \tag{3.21}$$

Also, from the way fitness values are mapped onto the roulette wheel, RWS leads to maximisation of the objective function if the values produced by the latter are taken as the fitness values. This leads to the need to scale the values produced by the objective function. [41]. For the purpose of this thesis, equation (3.20) must be minimised, so $G_{\mathrm{FROG}}(j)$ is scaled linearly such that

$$f(j) = G_{\mathrm{FROG}}(\mathrm{j}_{\max}) - G_{\mathrm{FROG}}(j), \tag{3.22}$$

where $j = \mathrm{j}_{\max}$ is the index for the largest value in $G_{\mathrm{FROG}}(j)$. By scaling $G_{\mathrm{FROG}}(j)$ in this fashion the least fit individual, i.e. the one with the highest $G_{\mathrm{FROG}}(j)$ value, is automatically removed from mating at each iteration of the GA.

Conversely, the best individual can automatically be selected into the mating pool, and, further, pass on to the next GA generation unaltered. This scheme is known as elitism and it was also implemented following [21].

PS methods such as RWS favour fitter individuals, allowing exploitation to dominate which leads to a comparatively faster decline in population diversity and hence to premature convergence. RS was proposed by [42], as a way to avoid premature convergence due to fitter individuals dominating the selection process. In this scheme, individuals are assigned a rank $rank(j)$, 1 for the least fit, J for the fittest, and the selection probability determined as follows

$$p_s(j) = \frac{a + (b-a)\frac{rank(j)-1}{J-1}}{\mathrm{J}}, \tag{3.23}$$

where a is the expected number of occurrences of the lowest ranked individual, set to 0.9 following [42], and b the expected number of occurrences of the highest ranked individual, such that $a+b = 2$ (so that $\sum_{j=1}^{J} p_s(j) = 1$). RS was the selection method employed in the GA created for this thesis following [19, 21].

Crossover

Once `mpool(q,p)` has been generated information is shared between chromosomes through Crossover. While q ranges from 1 to $Q = I$, the upper bound for $p = P$ is determined by the Crossover mechanism. Arithmetic Crossover was employed so $P = J$ [37]. This crossover operator operates on pairs of chromosomes, selected with equal probability p_c, which was set to 0.66 following [21].

Arithmetic Crossover combines two chromosomes a and b in a randomly selected pair yielding two

new chromosomes c and d such that

$$\begin{aligned} \Phi_i^c &= \alpha\Phi_i^a + (1-\alpha)\Phi_i^b, \\ \Phi_i^d &= (1-\alpha)\Phi_i^a + \alpha\Phi_i^b, \end{aligned} \tag{3.24}$$

The chromosomes in the pairs which are not selected for crossover remain in the population.

Mutation

Once the offspring has been generated random genes are selected with equal probability, p_m which was set to 0.01 following [21]. The selected genes are mutated with the aim of maintaining diversity in the population, without transforming the GA into a random search (which is why $p_m \ll p_c$), counteracting any loss of information caused by the Selection and Crossover operators [43].
Gaussian mutation was used such that

$$\Phi_i^j = \Phi_i^j + \eta, \tag{3.25}$$

where η is a random number taken from a gaussian distribution, with unity normalisation, a zero average and a standard deviation of 0.066 [21].

Chapter 4

Results and Discussion

4.1 Testing the Genetic Algorithm

All GA testing was carried out using 128×128 noise-free FROG traces. The trace size was selected to allow the characterization of pulses with a higher TBP than those tested by Vrany et al. [21], who used 64×64 traces for fibre-FROG, and to allow some measure of comparison of the GA's performance relative to the results obtained by Nicholson et al. [19], who used 128×128 traces and SHG-FROG. To further ensure an equivalent ground for comparing the GA's performance the algorithm was run for a fixed number of iterations, $K = 32000$, with $J = 32$ chromosomes.
All test pulses were constructed as follows:

$$E_{u,v}(t) = \sqrt{I_u(t)}\, \mathrm{e}^{i\phi_{u,v}(t)}, \tag{4.1}$$

where

$$I_u(t) = \sum_{w=1}^{W} A_w\, \mathrm{e}^{-\left(t-\tau_w\right)^2/2\sigma_w^2}, \tag{4.2}$$

and

$$\phi_{u,v}(t) = C_1 \left(\frac{t}{T}\right)^2 + C_2 \left(\frac{t}{T}\right)^3 + C_3 \left(\frac{t}{T}\right)^4 + S I_u(t). \tag{4.3}$$

The parameter T in equation 4.3 is the RMS temporal width for a single gaussian pulse with a full-width at half maximum of $2\sqrt{2\log(2)}T = 100\,\mathrm{fs}$. All σ_w in equation (4.2) were defined as a positive fraction of T. The parameter A_w, corresponding to the peak amplitude, was set to unity for $\sigma_w = T$, and all other A_w were defined as proper positive fractions. The delay parameter τ_w was set as a fraction of σ_w. Finally, all the resulting $I_u(t)$ were normalised to $E_\mathrm{T} = 24\,\mathrm{pJ}$ following the discussion in §3.2.

Table 4.1: Test amplitude parameters.

u	A_1	A_2	A_3	A_4	A_5	τ_1	τ_2	τ_3	τ_4	τ_5	σ_1	σ_2	σ_3	σ_4	σ_5
1	1.0	0	0	0	0	0	0	0	0	0	1.0	0	0	0	0
2	0.05	1.0	0.04	0	0	-6.8	0	6.5	0	0	0.53	0.9	0.51	0	0
3	0.31	0.45	1.0	0.51	0.23	-7.1	-4.7	0	4.1	7.2	0.75	0.74	1.0	0.51	0.23

The upper bound for the coefficients C_1, C_2, C_3 and S was set by ensuring $E_{u,v}(\omega)$ was contained within the spectral range and the FSR was obeyed for the FROG traces generated from $E_{u,v}(t)$. Following the discussion in §3.2 the time step used in creating the pulses was $\Delta t = 14.2\,\mathrm{fs}$ so that $t_{\mathrm{range}} = 1.8\,\mathrm{ps}$ for $N = 128$.

Table 4.2: Test phase parameters.

v	C_1	C_2	C_3	S
1	-0.2	0	0	0
2	0.2	0	0	0
3	0	0	0	0.009
4	0	-0.02	0	0
5	0	0.02	0	0
6	0.2	0.002	0.00001	0.009

Initially, three pulses of increasing TBP, $E_{1,1}$, $E_{2,1}$ and $E_{3,1}$, (cf. table 4.3) were used to the test fibre-FROG reconstruction. The TBP was varied by varying the pulse amplitude while the negative quadratic phase remained constant (cf. tables 4.1 and 4.2).

Table 4.3: Test pulse complexity, $G_{\mathrm{fibre-FROG}}$ and multi-objective function parameters.

Pulse	TBP	$G_{\mathrm{fibre-FROG}}$	$G_{\mathrm{PG-FROG}}$	fibre-FSR	Z_1	Z_2	Seed Pair
$E_{1,1}$	0.640	1.040×10^{-4}	8.962×10^{-6}	42	0.9	0.1	1
$E_{2,1}$	1.563	1.704×10^{-4}	4.619×10^{-5}	18	0.9	0.1	1
$E_{3,1}$	7.047	2.313×10^{-4}	1.284×10^{-4}	12	0.9	0.1	1
$E_{2,2}$	1.563	2.037×10^{-3}	4.039×10^{-5}	18	0.5	0.5	1
$E_{2,3}$	2.027	2.479×10^{-4}	5.201×10^{-5}	16	0.5	0.5	1
$E_{2,4}$	1.554	1.166×10^{-3}	1.498×10^{-5}	17	0.5	0.5	1
$E_{2,5}$	1.554	1.019×10^{-4}	1.205×10^{-5}	17	0.5	0.5	2
$E_{1,2}$	0.640	3.698×10^{-5}	8.832×10^{-6}	44	0.5	0.5	3
$E_{2,6}$	1.947	3.312×10^{-4}	6.095×10^{-5}	16	0.9	0.1	1

As the reconstruction of $E_{1,1}$, $E_{2,1}$ and $E_{3,1}$ was initially unsuccessful (cf. figure 4.1(b), 4.1(d) and 4.1(f)) the GA was tested for the same pulses using the PG-FROG geometry (cf. table 3.1). As these new tests were successful it was posited that the difference in results might be related to the PG-FROG traces producing a more adequate time-frequency representation of the test pulses. In particular, the fibre-FROG traces do not have finite support in the time-domain due to the form of $E_{\mathrm{sig}}^{\mathrm{fibre-FROG}}(t,\tau)$. This means fibre-FROG traces cannot possibly obey the FSR in the time-domain.
Looking at the exponent in $E_{\mathrm{sig}}^{\mathrm{fibre-FROG}}(t,\tau)$ it is noted that $I_{\mathrm{FROG}}(\omega,\tau)$ is constant for large and small values of τ, for temporal windows of arbitrary size, so this information can in principle be extracted from $I_{\mathrm{FROG}}(\omega,\tau)$. To this end a fibre-FSR conditon was proposed such that

$$\left| 1 - \frac{I_{\mathrm{FROG}}^{\max}(\omega, \tau = (\mp N/2 \pm z)\Delta t)}{I_{\mathrm{FROG}}^{\max}(\omega, \tau = \mp \Delta t N/2)} \right| \leq 10^{-4}. \tag{4.4}$$

This condition measures the absolute value of the difference between $I^{\max}_{\text{FROG}}(\omega, \tau = \mp\Delta t N/2)$, the maximum intensity at either edge of the time domain, and $I^{\max}_{\text{FROG}}(\omega, \tau = (\mp N/2 \pm z)\Delta t)$, the maximum intensity at $\tau = \pm z\Delta t$ from either edge of the time domain, relative to the former. The fibre-FSR is defined as the maximum number of points z which yield a delay where the fibre-FSR condition is obeyed.

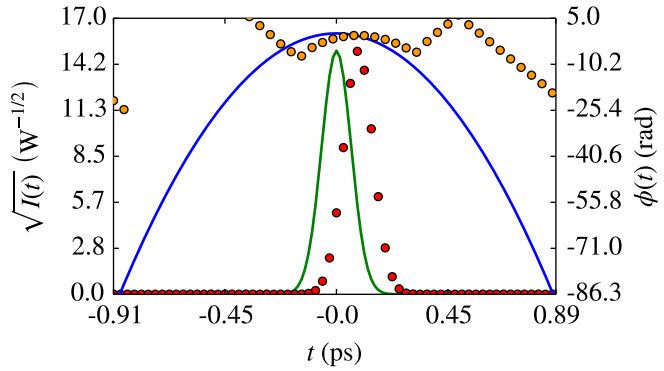

(a) Reconstruction for test pulse $E_{1,1} = E^*_{1,2}$.

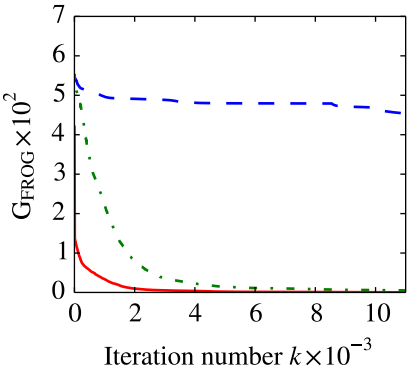

(b) GA convergence for test pulse $E_{1,1}$.

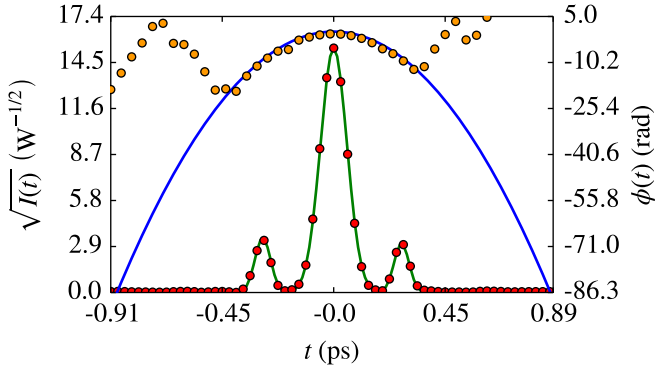

(c) Reconstruction for test pulse $E_{2,1} = E^*_{2,2}$.

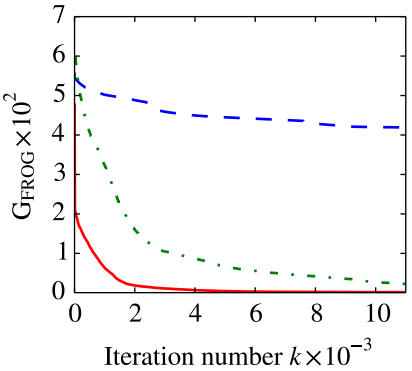

(d) GA convergence for test pulse $E_{1,1}$.

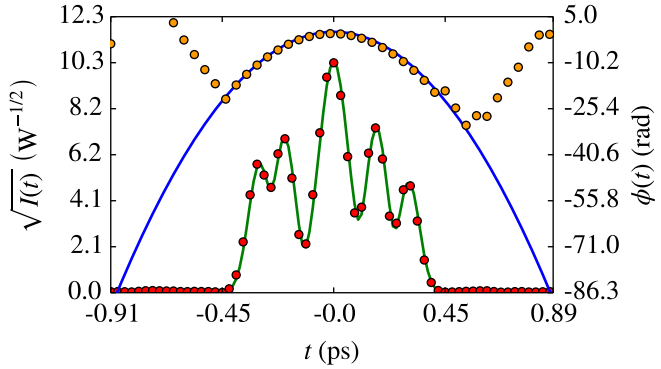

(e) Reconstruction for test pulse $E_{3,1}$.

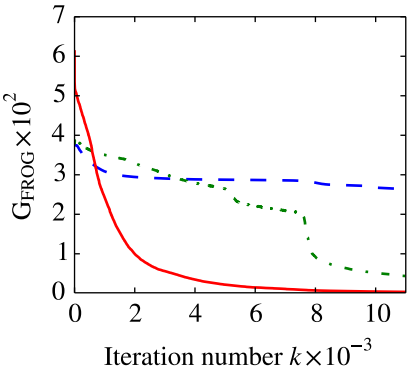

(f) GA convergence for test pulse $E_{3,1}$.

Figure 4.1: Figures **(a)**, **(c)** and **(e)** show exact and reconstructed amplitudes (solid green line and red circular markers respectively), and phases (solid blue line and orange circular markers respectively), for pulses $E_{1,1} = E^*_{1,2}$, $E_{2,1} = E^*_{2,2}$ and $E_{3,1}$. Correspondingly, figures **(b)**, **(d)** and **(f)** show the GA's convergence over the first 10×10^3 iterations for PG-FROG (solid red line), fibre-FROG with (dash-dotted green line) and without (dashed blue line) the fibre-FSR condition. Note the temporal shift in the reconstruction in figure**(a)**.

The fibre-FSR is assumed equal on both sides of the pulse but this can easily be adjusted to compensate for any asymmetries in $E_{\text{sig}}^{\text{fibre-FROG}}(\omega,\tau)$ along τ. Using the fibre-FSR the following modification of the GA's objective function was proposed,

$$G_{\text{FROG}}(j) \rightarrow Z_1 G_{\text{FROG}}(j) + Z_2 F(j), \tag{4.5}$$

where Z_1 and Z_2 are constants. Specifically, the information in the fibre-FSR is used so that $F(j) = \sum_{i=\mp N/2}^{\pm z} |E_i^j|^2/E_{\text{T}}$. In essence, the fibre-FSR is used to create a multi-objective fitness function that minimises G_{FROG} while also minimising the energy of the pulses corresponding to each chromosome (trial-phase) at the edges of the time domain. The second attempt at the fibre-FROG reconstruction of test pulses $E_{1,1}$, $E_{2,1}$ and $E_{3,1}$ was successful and the results presented in figures 4.1(a), 4.1(c) and 4.1(e) respectively. All three reconstructions were successful using the fibre-FSR condition yet the rate of convergence over the first 10000 iterations was distinctly lower than that for PG-FRO, (cf. figures 4.1(b), 4.1(d) and 4.1(f)). The final $G_{\text{fibre-FROG}}$ was at least an order of magnitude greater than $G_{\text{PG-FROG}}$, except for $E_{3,1}$ where of the same order, as shown in table 4.3.

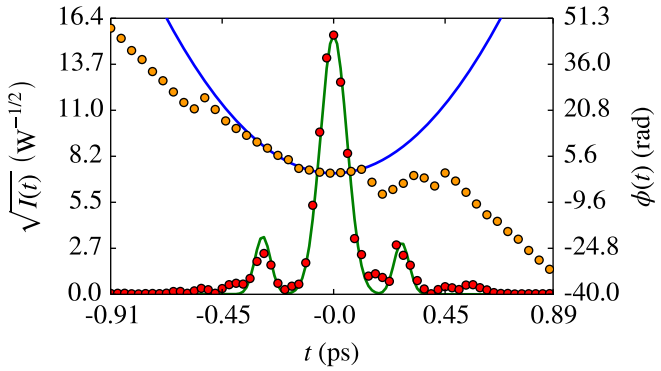

(a) Reconstruction for test pulse $E_{2,2} = E_{2,1}^*$.

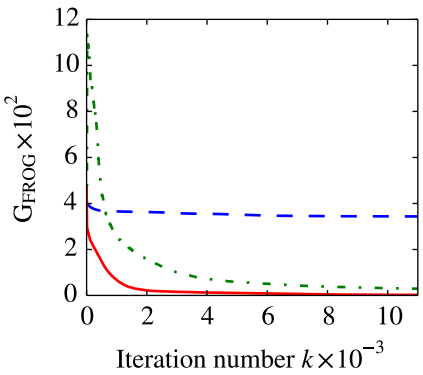

(b) GA convergence for test pulse $E_{2,2}$.

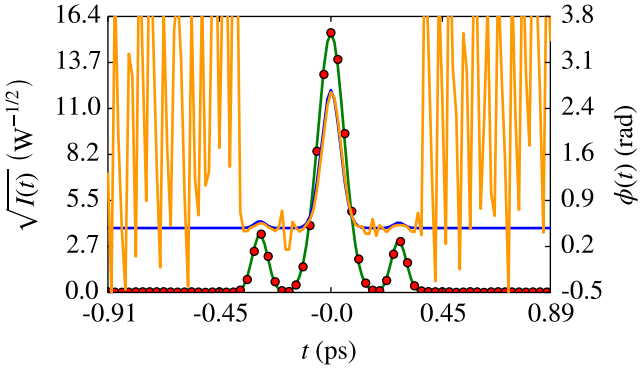

(c) Reconstruction for test pulse $E_{2,3}$.

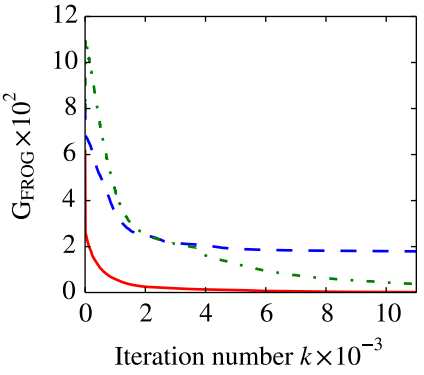

(d) GA convergence for test pulse $E_{2,3}$.

Figure 4.2: Figures **(a)**, **(c)** show exact and reconstructed amplitudes (solid green line and red circular markers respectively), and phases (solid blue and orange lines respectively), for pulses $E_{2,2} = E_{2,1}^*$ and $E_{2,3}$. Correspondingly, figures **(b)** and **(d)** show the GA's convergence over the first 10×10^3 iterations for PG-FROG (solid red line), fibre-FROG with (dash-dotted green line) and without (dashed blue line) the fibre-FSR condition. The phase in figure **(c)** is wrapped.

In order to further test the GA using the multi-objective fitness function, pulse $E_{2,2} = E^*_{2,2}$ was created to test the effect of a change in phase sign, and pulse $E_{2,3}$ to test the effect of SPM. The reconstructions for these test pulses were successful, but parameters Z_1 and Z_2 were changed in order to achieve this (cf. table 4.3). It was also noted that the final $G_{\text{fibre-FROG}}$ for $E_{2,2} = E^*_{2,1}$ was two orders of magnitude higher than that for pulse $E_{2,1}$, and the differences in the accuracy of the reconstruction can be seen by comparing figures 4.1(c) and 4.2(a). Comparing the two input traces for these two pulses (cf. figures 4.4(c) on the next page and 4.3(a) below) shows they are very distinct, despite representing pulses with the same TBP. Furthermore, the PG-FROG input traces for the same pulses (cf. figures 4.4(c) on the next page and 4.3(a) below) have a clear symmetry between them, where the existence of satellite pulse structure is also made clear, as is the sign of the phase. Pulse $E_{2,3}$ was also successfully reconstructed, and its input trace, (cf. figure 4.3), was also more intuitive using PG-FROG, displaying the characteristic spectral broadening induced by SPM.

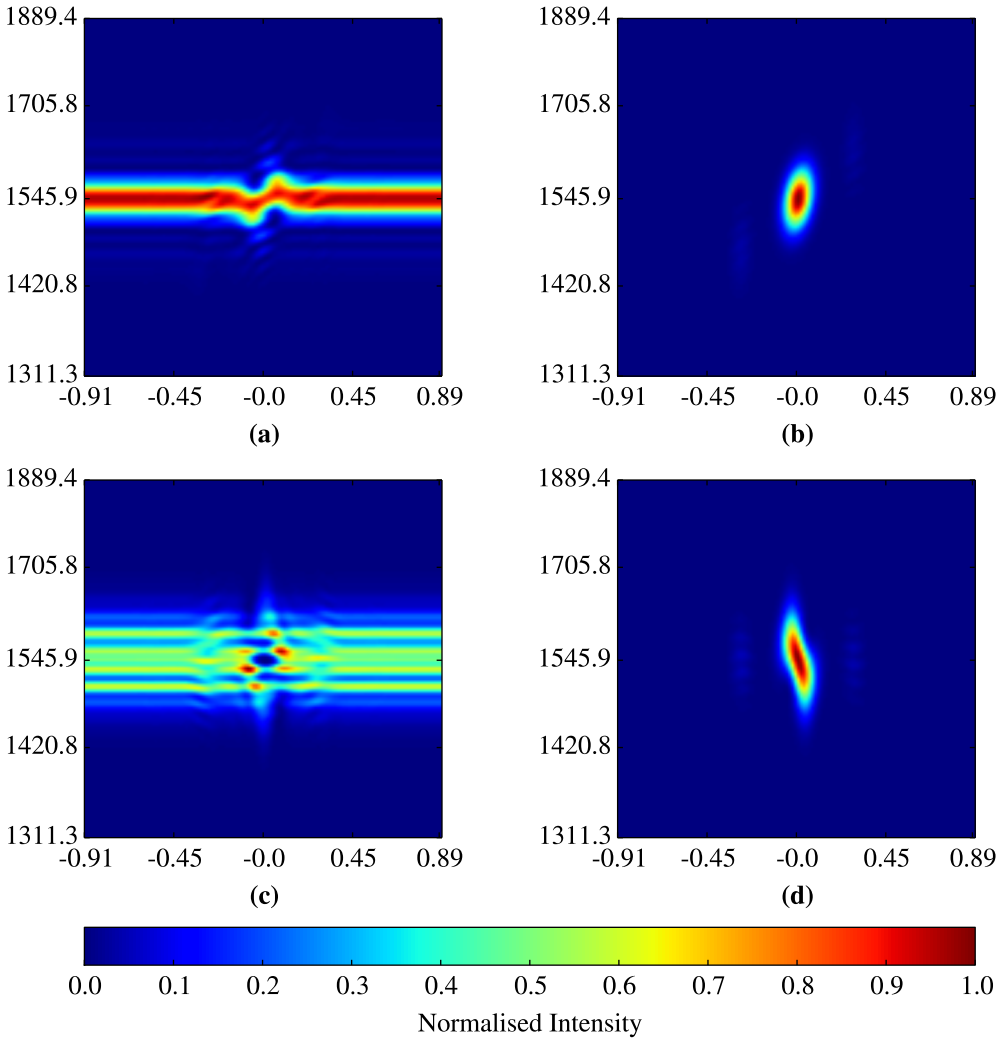

Figure 4.3: Initial FROG traces for test pulses $E_{2,2} = E^*_{2,1}$ and $E_{2,3}$ using fibre-FROG ((**a**) and (**c**)), and PG-FROG ((**b**) and (**d**)) respectively. The horizontal axes represent the time delay τ in ps and the vertical axes the unevenly spaced wavelength λ in nm. The intensity has been normalised to peak unity by dividing all intensity values by the maximum value.

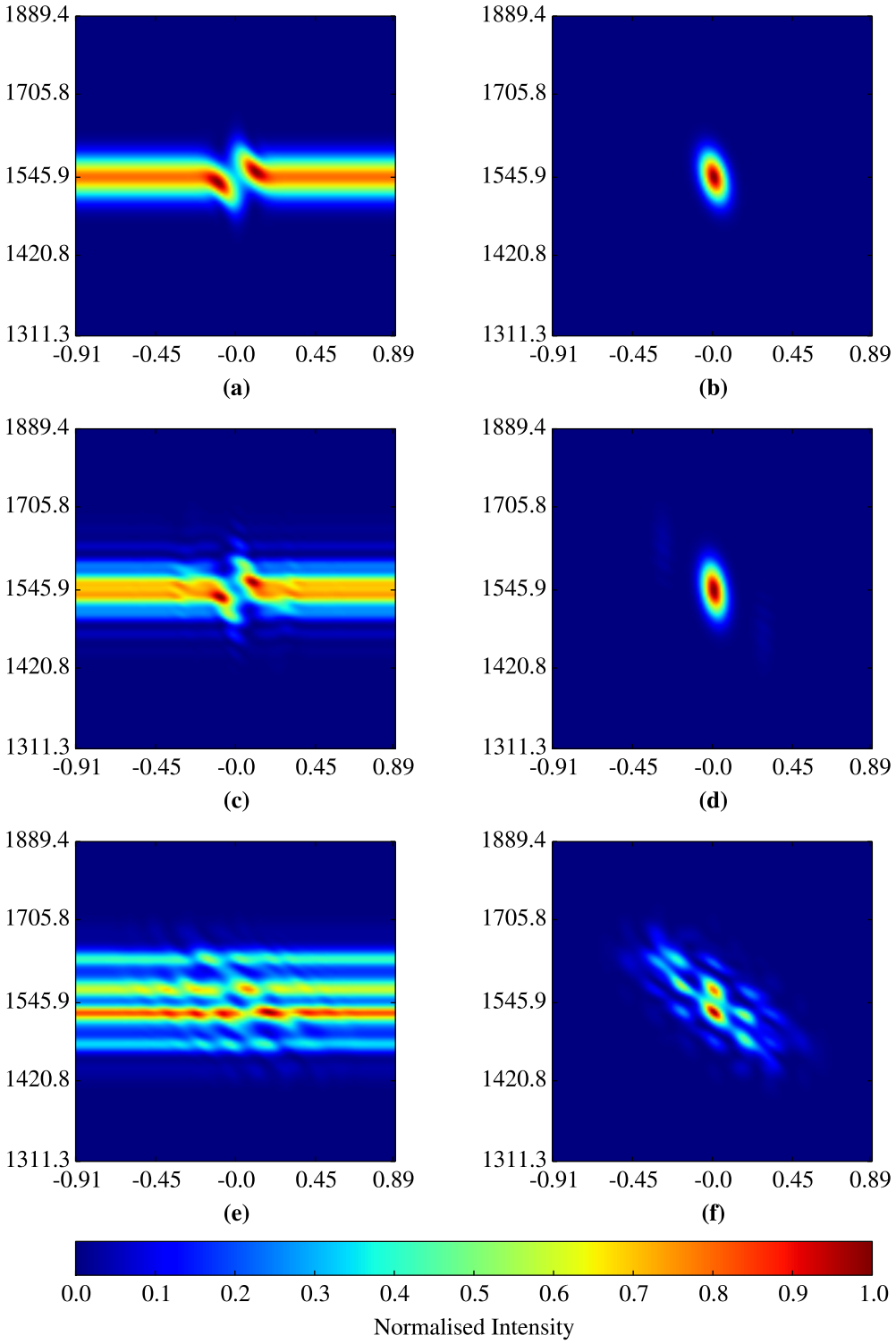

Figure 4.4: Initial FROG traces for test pulses $E_{1,1} = E^*_{1,6}$, $E_{2,1} = E^*_{2,2}$ and $E_{3,1}$ using fibre-FROG ((**a**),(**c**) and (**e**)), and PG-FROG ((**b**),(**d**) and (**f**)) respectively. The horizontal axes represent the time delay τ in ps and the vertical axes the unevenly spaced wavelength λ in nm. The intensity has been normalised to peak unity by dividing all intensity values by the maximum value.

The apparently unintuitive nature of the fibre-FROG input traces for pulses $E_{2,2}$ and $E_{2,1} = E^*_{2,2}$, the order of magnitude drop in the final value of $G_{\text{fibre-FROG}}$ from the latter to the former pulse, and the need to adjust coefficients Z_1 and Z_2 motivated the creation of two further test pulses: $E_{2,4}$ and $E_{2,5} = E^*_{2,4}$. Initially the coefficients Z_1 and Z_2 were the same, as those used in the successful reconstruction of pulses $E_{2,1}$ and $E_{2,2} = E^*_{2,1}$ (cf. table 4.3). Under those conditions only $E_{2,4}$ converged successfully, although the error in the reconstruction was noticeable, especially for $t < 0$, as can be seen in figure 4.5(a). Instead of altering Z_1 and Z_2 once more in order to achieve convergence for $E_{2,5} = E^*_{2,4}$, the seeds for the pseudo-random number generators in the algorithm were changed, and the reconstruction was successful (cf.figure 4.5(c)). The new seeds were also tested for $E_{2,4}$, unsuccessfully.

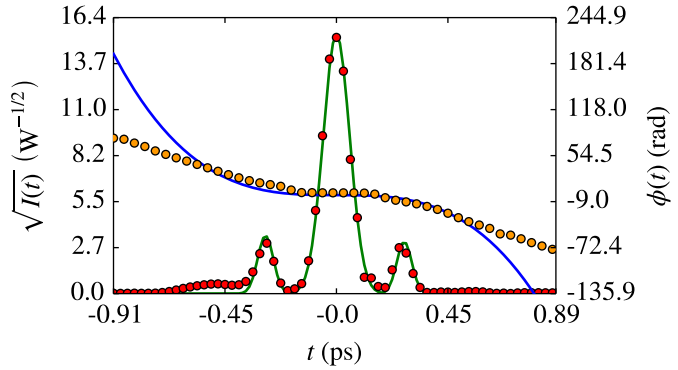

(a) Reconstruction for test pulse $E_{2,4}$.

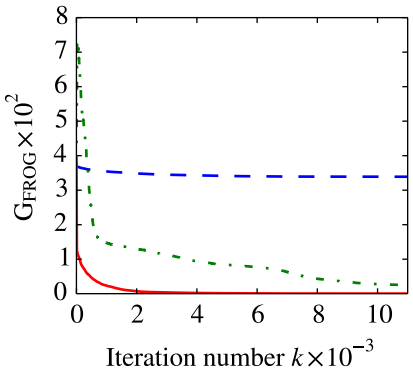

(b) GA convergence for test pulse $E_{2,4}$.

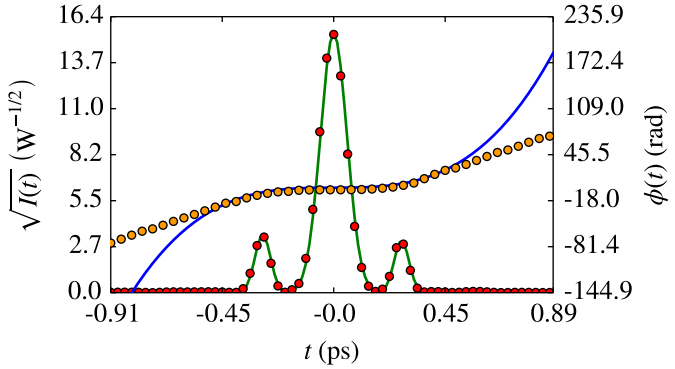

(c) Reconstruction for test pulse $E_{2,5} = E^*_{2,4}$.

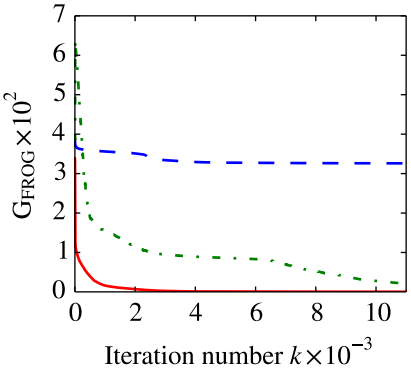

(d) GA convergence for test pulse $E_{2,5}$.

Figure 4.5: Figures **(a)**, **(c)** show exact and reconstructed amplitudes (solid green line and red circular markers respectively), and phases (solid blue and orange lines respectively), for pulses $E_{2,4}$ and $E_{2,5} = E^*_{2,4}$. Correspondingly, figures **(b)** and **(d)** show the GA's convergence over the first 10×10^3 iterations for PG-FROG (solid red line), fibre-FROG with (dash-dotted green line) and without (dashed blue line) the fibre-FSR condition.

Succinctly, two pulses with the same TBP and the same objective function required different seeds to achieve convergence. Each pulse was also reconstructed with PG-FROG, each using both seed pairs, and all reconstructions were successful.

The convergence of the PG-FROG reconstructions using the same seeds as the successful fibre-FROG reconstructions is presented in figures 4.5(b) and 4.5(d). It is noted that fibre-FROG convergence with the fibre-FSR behaves similarly for pulses $E_{2,4} = E^*_{2,5}$, $E_{2,3}$ and $E_{2,2}$, with a significant increase in

$G_{\text{fibre-FROG}}$ over approximately the first 10 iterations before it begins to decrease consistently. Finally, it is noted that unlike the fibre-FROG input traces for pulses $E_{2,1}$ and $E_{2,2} = E^*_{2,1}$, the input traces for pulses $E_{2,4}$ and $E_{2,5} = E^*_{2,4}$ display a clear 180° symmetry between them, as do the PG-FROG input traces (cf. figure 4.6), indicative of a change of sign in the phase.

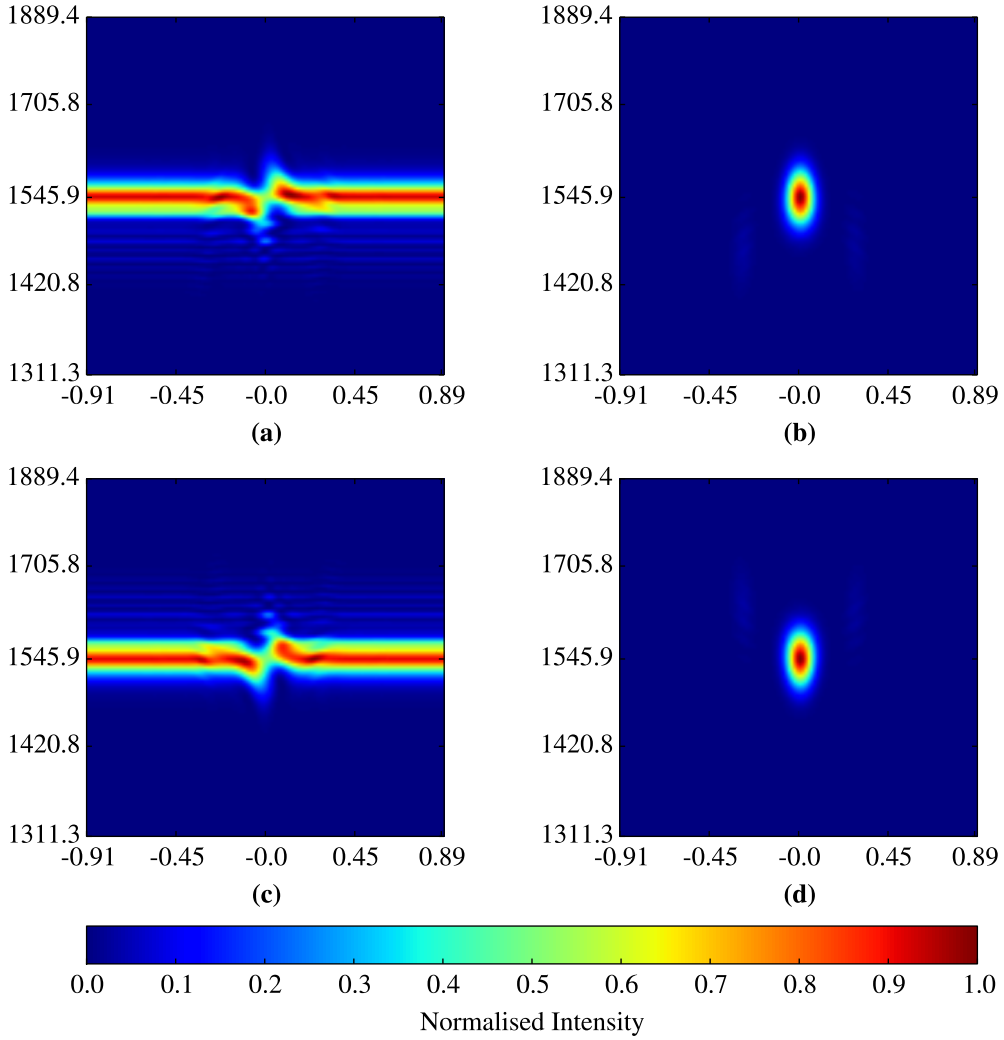

Figure 4.6: Initial FROG traces for test pulses $E_{2,4}$ and $E_{2,5} = E^*_{2,4}$ using fibre-FROG (**(a)** and **(c)**), and PG-FROG (**(b)** and **(d)**) respectively. The horizontal axes represent the time delay τ in ps and the vertical axes the unevenly spaced wavelength λ in nm. The intensity has been normalised to peak unity by dividing all intensity values by the maximum value.

The last two test pulses, $E_{1,2} = E^*_{1,1}$ and $E_{2,6}$ were created to further test the effect of a change in phase sign and of a mix of different phase terms respectively (cf. tables 4.3 and 4.2). The reconstruction of $E_{1,2}$ failed under the same conditions that enabled the successful reconstruction of $E_{1,1}$, and $E_{2,2}$. Comparing the fibre-FROG input traces for pulses $E_{1,1}$ and $E_{1,2}$ (cf. figures 4.4(a) and 4.7(a)), shows that, once more, the change of the quadratic phase sign produces no obvious symmetry between traces, as was the case with the input traces for pulses $E_{2,1}$ and $E_{2,2} = E^*_{2,1}$. A comparison of the fibre-FROG input traces for pulses $E_{1,2}$ and $E_{2,2}$ (cf. figure 4.3(b)) shows two distinct input

traces are generated, although the relative difference is not comparable to that of the respective PG-FROG input traces, especially given that the TBP for $E_{2,2}$ is about twice that of $E_{1,2}$. The successful reconstruction of pulse $E_{1,2}$ was achieved by selecting a new seed for the pseudo-random number generators. Finally, it is noted that the convergence of the reconstruction for pulse $E_{1,2}$ (cf. figure 4.8(b) on the next page) follows the same pattern over approximately the first 10 iterations as all the other reconstructions for pulses using the same objective function (cf. table 4.3) despite differences in phase, amplitude and the pseudo-random number generator seeds. Finally, it is noted that the PG-

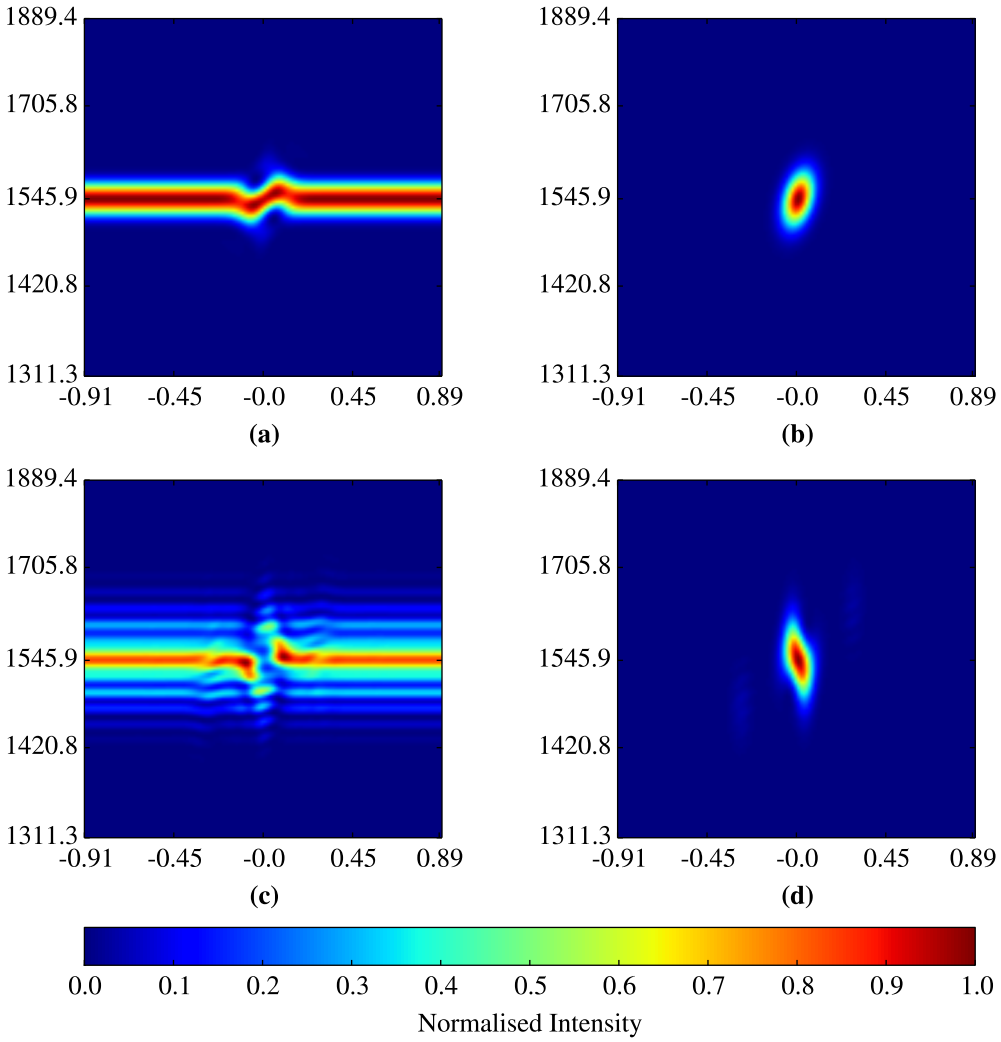

Figure 4.7: Initial FROG traces for test pulses $E_{1,2} = E^*_{1,1}$ and $E_{2,6}$ using fibre-FROG ((**a**),(**c**)), and PG-FROG ((**b**),(**d**)) respectively. The horizontal axes represent the time delay τ in ps and the vertical axes the unevenly spaced wavelength λ in nm. The intensity has been normalised to peak unity by dividing all intensity values by the maximum value.

FROG input trace for pulse $E_{1,6}$ displays information regarding the presence of an SPM phase term as well as of a positive quadratic phase term.

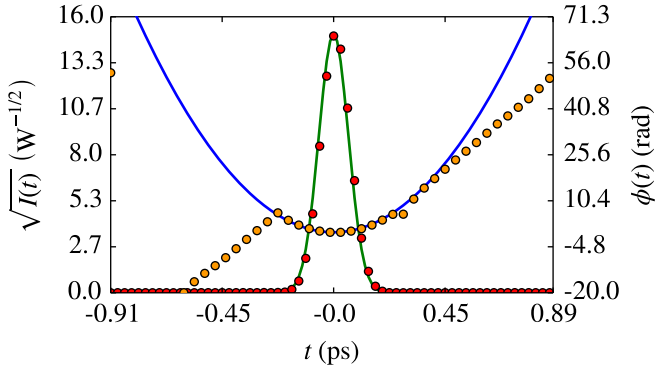

(a) Reconstruction for test pulse $E_{1,2} = E^*_{1,1}$.

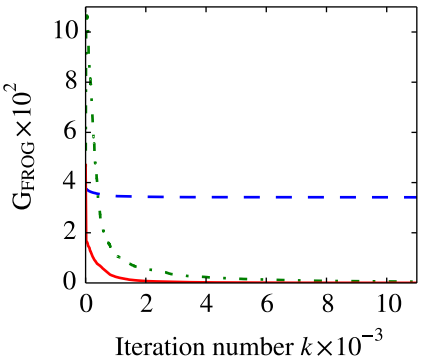

(b) GA convergence for test pulse $E_{1,2}$.

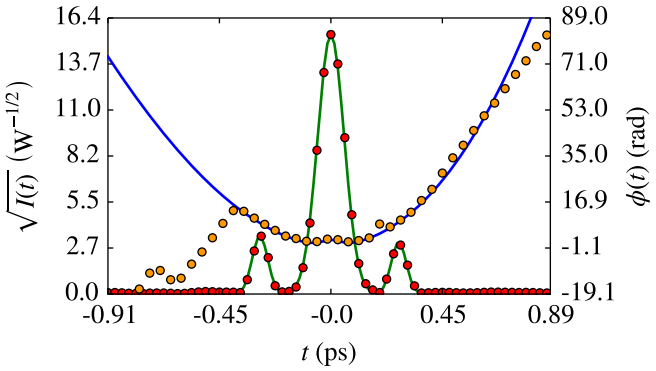

(c) Reconstruction for test pulse $E_{2,6}$.

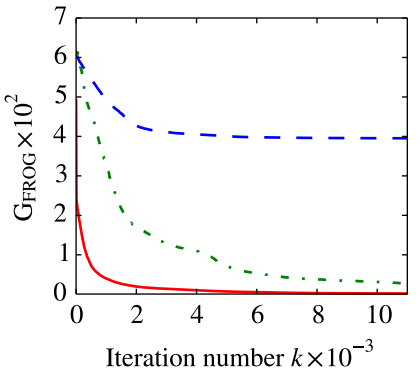

(d) GA convergence for test pulse $E_{2,6}$.

Figure 4.8: Figures **(a)**, **(c)** show exact and reconstructed amplitudes (solid green line and red circular markers respectively), and phases (solid blue and circular orange markers respectively), for pulses $E_{1,2} = E^*_{1,1}$ and $E_{2,6}$. Correspondingly, figures **(b)** and **(d)** show the GA's convergence over the first 10×10^3 iterations for PG-FROG (solid red line), fibre-FROG with (dash-dotted green line) and without (dashed blue line) the fibre-FSR condition.

4.2 Genetic Algorithm for fiber-FROG using Simulated Pulse Propagation

All the fibre-FROG reconstructions performed in §4.1 are performed ignoring the dispersive effects of the fibre, which yields an exact expression for $E_{\text{sig}}^{\text{fibre-FROG}}(t,\tau)$. For the available DSF, this was experimentally determined to be true around $\lambda = 1545.9\,\text{nm}$ (cf. figure 4.9). The pulse which was available for characterization had a spectrum centred around $\lambda = 1556\,\text{nm}$. Despite the DSF's relatively flat chromatic dispersion slope, (cf. 4.9(a)) from which it was calculated that $\beta_2 = -804.78\,\text{fs}^2\,\text{m}^{-1}$, dispersion becomes significant for pulses with temporal widths of the order of tens and hundreds of fs propagating over some metres of the DSF. In order to account for this, the GA was modified, using existing code for simulating pulse propagation in the amplitude's frame of reference, in order to solve the coupled propagation equations numerically, while performing the fibre-FROG phase reconstruction. Third order dispersion was also taken into account, $\beta_3 = 0.044\,15\,\text{fs}^3\,\text{m}^{-1}$ as well as fibre losses, $\alpha = 2.059\,\text{km}^{-1}$. The latter was obtained directly from the data in figure 4.9(d) and the former was calculated from the numerical derivative of $\beta_2(\omega)$, and presented in figure 4.9(c).

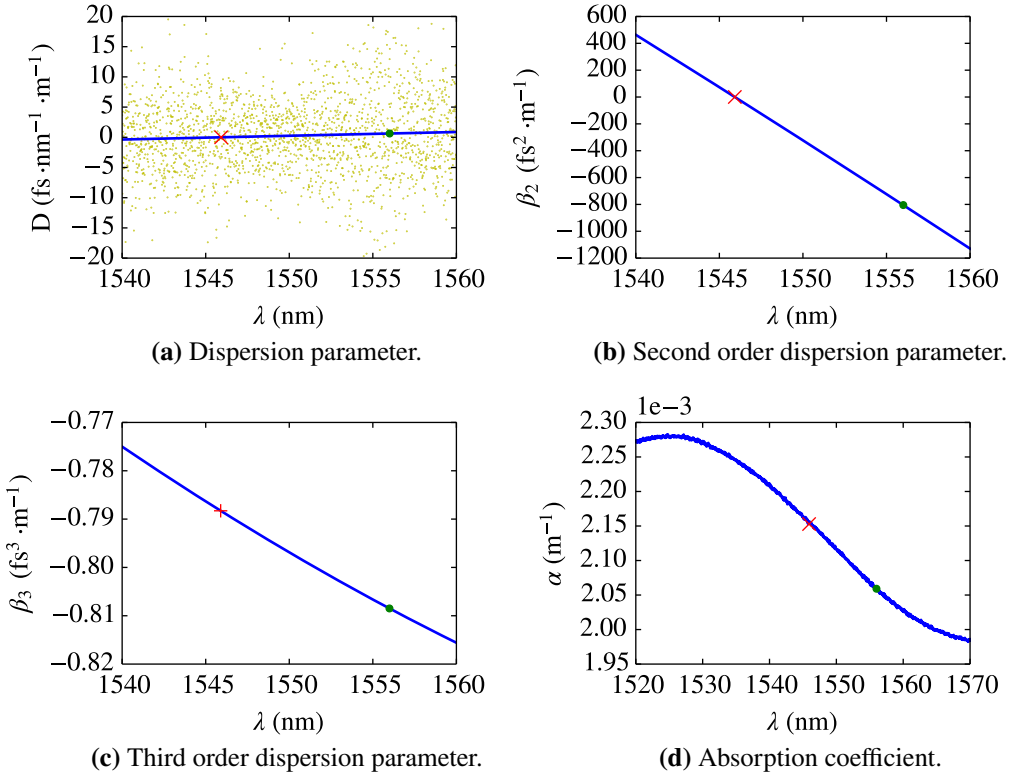

(a) Dispersion parameter.

(b) Second order dispersion parameter.

(c) Third order dispersion parameter.

(d) Absorption coefficient.

Figure 4.9: DSF experimental characterisation data. The red cross marks $\lambda = 1545.9\,\text{nm}$ (zero dispersion wavelength) and the green circle $\lambda = 1556\,\text{nm}$. The yellow markers in (a) are experimental data and the blue line is a linear interpolation of that data.

The pulses selected for this were $E_{1,1}$ and $E_{1,2} = E_{1,1}^*$ as they were the pulses with the smallest TBP. This was done to ensure that the output $E_{\text{sig}}^{\text{fibre-FROG}}(t,\tau)$ was well contained within the temporal window, for all values of τ. The pulse with the next highest TBP was also tested, but it was not contained within the temporal window. Comparing the input traces for $E_{1,1}$ and $E_{1,2} = E_{1,1}^*$, displayed in figures 4.10(a) 4.10(b), and comparing them with the corresponding traces for the non-dispersive regime (cf. figures 4.1(a) and 4.8(a)) shows they are distinct.

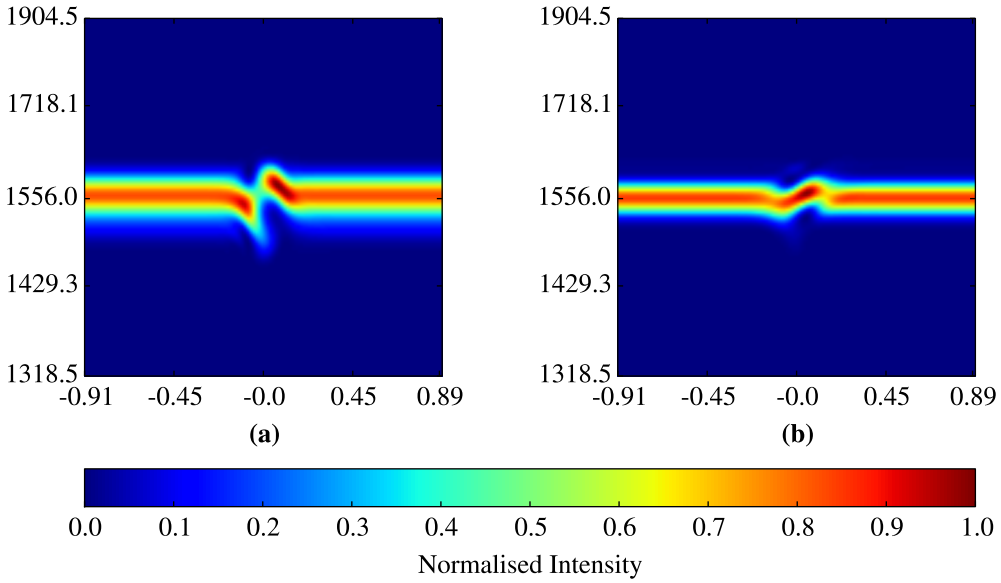

Figure 4.10: Initial FROG traces for test pulses $E_{1,1}$ and $E_{1,2} = E_{1,1}^*$ using fibre-FROG ((**a**) and(**b**)) and propagation simulation. The horizontal axes represent the time delay τ in ps and the vertical axes the unevenly spaced wavelength λ in nm. The intensity has been normalised to peak unity by dividing all intensity values by the maximum value.

The GA with propagation simulation ran for about 13 hours, compared to about 7 minutes without propagation simulation. The rate of convergence was slightly lower for the latter the former case (cf. figures 4.11(b) and 4.11(d)), and the final $G_{\text{fibre-FROG}}$ values were 3.089×10^{-5} and 2.792×10^{-5}, for pulses $E_{1,1}$ and $E_{1,2}$ respectively. Comparing these values with those in table 4.3 shows the propagation simulation produced a lower final $G_{\text{fibre-FROG}}$ in both cases. In both cases the reconstruction was carried out using the same objective function parameters as were used for the reconstruction with an exact expression for the signal.

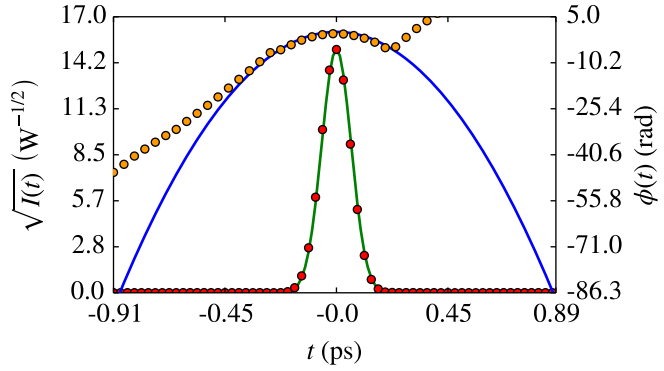

(a) Reconstruction for test pulse $E_{1,1}$.

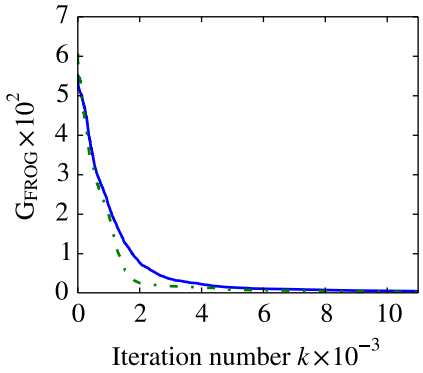

(b) GA convergence for test pulse $E_{1,1}$.

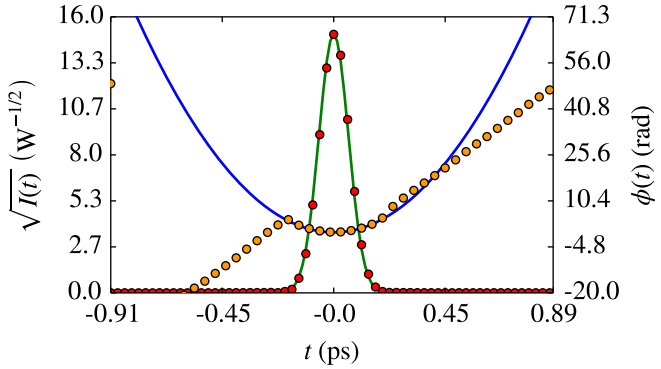

(c) Reconstruction for test pulse $E_{1,2} = E^*_{1,1}$.

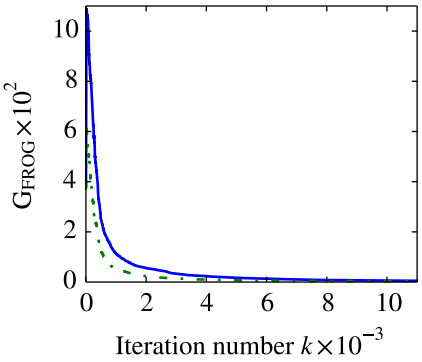

(d) GA convergence for test pulse $E_{1,2}$.

Figure 4.11: Figures **(a)**, **(c)** show exact and reconstructed amplitudes (solid green line and red circular markers respectively), and phases (solid blue and orange circular markers respectively), for pulses and using propagation simulation. Correspondingly, figures **(b)** and **(d)** show the GA's convergence over the first 10×10^3 iterations for fibre-FROG with (dash-dotted green line) and without (solid blue line) simulation propagation.

Chapter 5

Conclusion

The PG-FROG geometry generates more intuitive traces when compared to the fibre-FROG geometry, with information which is more localised in time and frequency, proportionally to the pulse's TBP. This is well understood by analysing $E_{\mathrm{SIG}}(t,\tau)$, where the trace $I_{\mathrm{FROG}}(\omega,\tau)$ is given by the modulus squared of the FT of $E(t)$ times the exponent of a phase term given by $\frac{i2\gamma L}{3}(|E(t)|^2+2\,|E(t-\tau)|^2)$. For $\tau \gg 0$ and $\tau \ll 0$ $E_{\mathrm{SIG}}(t,\tau) \approx E(t)\,\mathrm{e}\,\frac{i2\gamma L}{3}(|E(t)|^2$. This means the fibre-FROG trace cannot be localised in time.

A comparison of phase reconstructions for fibre-FROG and PG-FROG geometries using a GA showed that under the same parameters better reconstructions were obtained in the latter case. Intuitively this is understood from considering that information is better localised in a PG-FROG trace. As a GA is a directed random search, it is more likely to find a better optimum to a problem for an objective function which contains less possible optimization paths to search through. This notion is further supported by the fact that the final $G_{\mathrm{PG-FROG}}$ has a strong correlation with the pulse's TBP, and the latter with the region containing non-negligible intensity, as defined by the FSR condition introduced by Trebino [14].

In fact, it was observed that for all test pulses, with TBPs varying between 0.604 and 7.047, all fibre-FROG reconstructions were unsuccessful with final $G_{\mathrm{fibre-FROG}}$ values of the order of 10^{-2}. As long as $\tau \gg 0$ and $\tau \ll 0$ are such that $\frac{i2\gamma L}{3}\,|E(t)|^2$ dominates the behaviour of $E_{\mathrm{SIG}}(t,\tau)$ the trace should remain constant. Based on this, a measure of finite support was proposed for the temporal domain of the trace, termed the fibre-FSR. Employing the fibre-FSR, defined as the number of multiples of the time step Δt over which the fibre-FROG trace remains constant, a multi-objective function was introduced into the GA. The modified objective function was then used to simultaneously optimise $G_{\mathrm{fibre-FROG}}$, with weight Z_1, and the energy contained at the ends of the time domain chromosomes, with weight Z_2, at each iteration of the algorithm.

Using the two weights/parameters Z_1 and Z_2 all fibre-FROG reconstructions were performed successfully. However, two different sets of parameters Z_1 and Z_2 were used as well as three difference sets of seeds for the algorithm's random number generators. The need for different seeds was also reported by Vrany et al. [21]. One set of parameters $(Z_1, Z_2) = (0.1, 0.9)$ worked best for pulses whose traces had their intensity more widely distributed about the central frequency, while another, $(Z_1, Z_2) = (0.5, 0.5)$ worked best for pulses whose intensity was narrowly distributed around the cent-

ral frequency. One notable exception was the reconstruction of a test pulse with an SPM phase term. As these sets were independent of the seeds which were used, and of the pulse's TBPs, future work to determine optimal (Z_1, Z_2) pairs may prove worthwhile. Nonetheless, the multi-objective function proved successful in reconstructing the phases of the 9 test pulses, including an SPM phase, which Vrany et al. [21] had reported some difficulty with.

Finally, two of the test pulses, gaussians with a temporal RMS width of 100 fs and quadratic phases of opposite signs, with a TBP of 0.604, were successfully reconstructed using propagation simulation to account for the effect of dispersion over a 2 m of DSF fibre with a nonlinear coefficient $\gamma = 2.36\,\mathrm{W}^{-1}\,\mathrm{m}^{-1}$ and a pulse energy of 24 pJ. The effects of birefringence were not taken into account. As birefringence is significant over short lengths of low birefringence fibres [29] this may also be the object of future work for someone looking to apply fibre-FROG to characterise femtosecond pulses at wavelengths far from the fibre's zero-dispersion length.

Bibliography

[1] P. M. W. French. “The generation of ultrashort laser pulses”. In: *Reports on Progress in Physics* 58.2 (1995), p. 169.

[2] R. Kienberger et al. “Atomic transient recorder”. In: *Nature* 427.6977 (02/26/2004), pp. 817–821.

[3] A. Sabbah et al. “Femtosecond pump-probe reflectivity study of silicon carrier dynamics”. In: *Physical Review B* 66.16 (10/2002).

[4] Fausto Rossi et al. “Theory of ultrafast phenomena in photoexcited semiconductors”. In: *Reviews of Modern Physics* 74.3 (2002), p. 895.

[5] Samir Kumar Pal et al. “Biological Water: Femtosecond Dynamics of Macromolecular Hydration”. In: *The Journal of Physical Chemistry B* 106.48 (12/2002), pp. 12376–12395.

[6] Tobias Brixner et al. “Two-dimensional spectroscopy of electronic couplings in photosynthesis”. In: *Nature* 434.7033 (03/31/2005), pp. 625–628.

[7] J. Mauritsson et al. “Attosecond Electron Spectroscopy Using a Novel Interferometric Pump-Probe Technique”. In: *Physical Review Letters* 105.5 (07/2010).

[8] M. D. Thomson et al. “Complete pulse characterization at 1.5 μm by cross-phase modulation in optical fibers”. In: *Optics letters* 23.20 (1998), pp. 1582–1584.

[9] D. Cotter. “Fibre nonlinearities in optical communications”. In: *Optical and quantum electronics* 19.1 (1987), pp. 1–17.

[10] Günter Steinmeyer. “A review of ultrafast optics and optoelectronics”. In: *Journal of Optics A: Pure and Applied Optics* 5.1 (2003), R1.

[11] Andrew M. Weiner. “Ultrafast optical pulse shaping: A tutorial review”. In: *Optics Communications* 284.15 (2011), pp. 3669–3692.

[12] Hans-Georg Weber et al. “Ultrahigh-Speed OTDM-Transmission Technology”. In: *Journal of Lightwave Technology* 24.12 (12/2006), pp. 4616–4627.

[13] C. W. Berry et al. “Significant performance enhancement in photoconductive terahertz optoelectronics by incorporating plasmonic contact electrodes”. In: *Nature Communications* 4 (03/27/2013), p. 1622.

[14] Rick Trebino. *Frequency-resolved optical gating: the measurement of ultrashort laser pulses*. Vol. 1. Springer, 2000.

[15] Rick Trebino et al. “Using phase retrieval to measure the intensity and phase of ultrashort pulses: frequency-resolved optical gating”. In: *JOSA A* 10.5 (1993), pp. 1101–1111.

[16] Rick Trebino et al. “Measuring ultrashort laser pulses in the time-frequency domain using frequency-resolved optical gating”. In: *Review of Scientific Instruments* 68.9 (1997), p. 3277.

[17] Kenneth W. DeLong et al. “Improved ultrashort pulse-retrieval algorithm for frequency-resolved optical gating”. In: *JOSA A* 11.9 (1994), pp. 2429–2437.

[18] Eitan Yudilevich et al. “Restoration of signals from their signed Fourier-transform magnitude by the method of generalized projections”. In: *JOSA A* 4.1 (1987), pp. 236–246.

[19] J. W. Nicholson et al. “Evolving FROGS: phase retrieval from frequency-resolved optical gating measurements by use of genetic algorithms”. In: *Optics letters* 24.7 (1999), pp. 490–492.

[20] Daniel J. Kane. “Principal components generalized projections: a review [Invited]”. In: *Journal of the Optical Society of America B* 25.6 (06/01/2008), A120–A132.

[21] Boleslav Vrany et al. “Optimization of genetic algorithm for reconstruction of cross-phase modulation frequency-resolved optical gating data”. In: *International Journal of Numerical Modelling: Electronic Networks, Devices and Fields* 24.5 (2011), pp. 448–456.

[22] Chi Zhang et al. “High-sensitivity polarization gating frequency-resolved optical gating (PG-FROG) using highly-nonlinear dispersion-shifted fiber”. In: *OptoeElectronics and Communications Conference (OECC), 2011 16th*. IEEE, 2011, pp. 325–326.

[23] Dennis Gabor. “Theory of communication. Part 1: The analysis of information”. In: *Journal of the Institution of Electrical Engineers-Part III: Radio and Communication Engineering* 93.26 (1946), pp. 429–441.

[24] Boualem Boashash. *Time frequency analysis*. Gulf Professional Publishing, 2003.

[25] Leon Cohen. *Time-frequency Analysis: Theory and Applications*. Upper Saddle River, NJ, USA: Prentice-Hall, Inc., 1995.

[26] Leon Cohen. “Time-frequency distributions-a review”. In: *Proceedings of the IEEE* 77.7 (1989), pp. 941–981.

[27] Antoine Monmayrant et al. “A newcomer’s guide to ultrashort pulse shaping and characterization”. In: *Journal of Physics B: Atomic, Molecular and Optical Physics* 43.10 (05/28/2010), p. 103001.

[28] Paul N. Butcher et al. *The Elements of Nonlinear Optics*. Cambridge University Press, 07/26/1991. 364 pp.

[29] Govind P. Agrawal. *Nonlinear fiber optics*. Springer, 2000.

[30] John A. Buck. *Fundamentals of optical fibers*. John Wiley & Sons, 2004.

[31] K.W. DeLong et al. “Practical issues in ultrashort-laser-pulse measurement using frequency-resolved optical gating”. In: *IEEE Journal of Quantum Electronics* 32.7 (07/1996), pp. 1253–1264.

[32] Nuno Alexandre Silva et al. “Effective Nonlinear Parameter Measurement Using FWM in Optical Fibers in a Low Power Regime”. In: *IEEE Journal of Quantum Electronics* 46.3 (03/2010), pp. 285–291.

[33] Kenneth W. DeLong et al. “Pulse retrieval in frequency-resolved optical gating based on the method of generalized projections”. In: *Optics letters* 19.24 (1994), pp. 2152–2154.

[34] Lina Xu et al. “Simulations of frequency-resolved optical gating for measuring very complex pulses”. In: *JOSA B* 25.6 (2008), A70–A80.

[35] Darrell Whitley. “A genetic algorithm tutorial”. In: *Statistics and computing* 4.2 (1994), pp. 65–85.

[36] Mitchell Melanie. *An introduction to genetic algorithms*. Vol. 3. 1999.

[37] Francisco Herrera et al. “Tackling real-coded genetic algorithms: Operators and tools for behavioural analysis”. In: *Artificial intelligence review* 12.4 (1998), pp. 265–319.

[38] David E. Goldberg. “Real-coded genetic algorithms, virtual alphabets, and blocking”. In: *Urbana* 51 (1990), p. 61801.

[39] Matej Črepinšek et al. “Exploration and Exploitation in Evolutionary Algorithms: A Survey”. In: *ACM Comput. Surv.* 45.3 (07/2013), 35:1–35:33.

[40] David E. Goldberg et al. “A comparative analysis of selection schemes used in genetic algorithms”. In: *Urbana* 51 (1991), pp. 61801–2996.

[41] Vladik Kreinovich et al. “Genetic algorithms: what fitness scaling is optimal?” In: *Cybernetics and Systems* 24.1 (1993), pp. 9–26.

[42] James Edward Baker. “Adaptive selection methods for genetic algorithms”. In: *Proceedings of an International Conference on Genetic Algorithms and their applications*. Hillsdale, New Jersey, 1985, pp. 101–111.

[43] David M. Tate et al. “Expected Allele Coverage and the Role of Mutation in Genetic Algorithms.” In: *ICGA*. 1993, pp. 31–37.